12-2019

Interfacial Contact with Noble Metal - Noble Metal and Noble Metal - 2D Semiconductor Nanostructures Enhance Optical Activity

Ricardo Raphael Lopez Romo
University of Arkansas, Fayetteville

Interfacial Contact with Noble Metal - Noble Metal and Noble Metal - 2D Semiconductor Nanostructures Enhance Optical Activity

A thesis submitted in partial fulfillment
of the requirements for the degree of
Master of Science in Microelectronics-Photonics

by

Ricardo R. L. Romo
Southern Arkansas University
Bachelor of Science in Engineering Physics 2016

December 2019
University of Arkansas

This thesis is approved for recommendation to the Graduate Council.

_____
D. Keith Roper, Ph.D.
Thesis Director

_____
Ryan Tian, Ph.D
Committee Member

_____
Lauren Greenlee, Ph.D
Committee Member

_____
Rick Wise, Ph.D
Ex-Officio Member

The following signatories attest that all software used in this thesis was legally licensed for use by Mr. Ricardo Romo for research purposes and publication.

Mr. Ricardo Romo Student	Dr. D. Keith Roper Thesis Director

This thesis was submitted to http:/ww.turnitin.com for plagiarism review by the TurnItIn company's software. The signatories have examined the report on this thesis that was returned by Turnitin and attest that in their opinion, the items highlighted by the software are incidental to common usage and are not plagiarized material.

Dr. Rick Wise Program Director	Dr. D. Keith Roper Thesis Director

Abstract

Noble metal nanoparticles and two-dimensional (2D) transition metal dichalcogenide (TMD) crystals offer unique optical and electronic properties that include strong exciton binding, spin-orbital coupling, and localized surface plasmon resonance. Controlling these properties at high spatiotemporal resolution can support emerging optoelectronic coupling and enhanced optical features. Excitation dynamics of these optical properties on physicochemically bonded mono- and few-layer TMD crystals with metal nanocrystals and two overlapping spherical metal nanocrystals were examined by concurrently (i) DDA simulations and (ii) far-field optical transmission UV-vis spectroscopic measurements. Initially, a novel and scalable method to unsettle van der Waals bonds in bulk TMDs to prepare mono- and few-layer crystals was performed. Examination of the solution-based and electrochemical deposition of metal nanocrystals on 2D TMD crystals, comparing their optical, electronic, and optoelectronic characteristics was accomplished via characterization methods. Subsequently, DDA simulations for noble metal - semiconductor nanocrystal and noble metal - noble metal nanocrystal heterostructures analyzed the effects of metal type, geometry, and orientation for the predefined nanoantennae parameters. Results from these computational and experimental optical spectra demonstrate promising percent error difference, in which distinguished quantitative effects of 2D TMDs crystals - metal nanocrystals and metal nanocrystals - metal nanocrystals facilitated optoelectronic activity in the UV-Vis-NIR region. New experimental and theoretical insights into energy conversion interactions between coupled plasmonic and excitonic materials spanning the optical regimes were established towards their applications in optoelectronic and biological engineering platforms.

Acknowledgments

In my graduate career, the guidance, mentorship, and support from many people have made it possible to accomplish this work. I would like to thank my advisor, Dr. Keith Roper, for his expertise, knowledge, guidance, and mentorship throughout my graduate career. I would also like to thank my committee members, Dr. Ryan Tian and Dr. Lauren Greenlee, for their participation and support for this work. Additionally, I would like to thank the MicroEP program (Dr. Rick Wise, Renee Hearon, Emily Ebbing, and others) for their invaluable time and effort they spent to assist me with finishing graduate school.

I would like to acknowledge and thank all the students that I built a strong collaborative relationship with during the time I was here. I have benefited and would like to acknowledge current and graduated students: Keith Berry, Vinith Bejugam, Gregory Forcherio, Jeremy Dunklin, Aida Sheibani, and Roy French who have made my time here invaluable. I would also like to thank the undergrads: Alex O'Brien, Autumn Lovelady, Michala Smith, Lauren Shepard, Hannah Thornton, Jacob Schmidt, Lina Patel, Arturo de la Vega, and Loc Huynh, who gave me the opportunity to mentor and them guide during my graduate career.

I am thankful to all of the faculty and staff in the Ralph E. Martin Department of Chemical Engineering and the Nanoscience and Engineering Institute at the University of Arkansas. I am also grateful for the University of Arkansas Foundation, the Walton Family Charitable Foundation, University of Arkansas Honors College Research Grant, and the Arkansas Biosciences Institute, the major research component of the Arkansas Tobacco Settlement Proceeds Act of 2000.

Lastly, I am truly grateful for my parents: Ricardo Romo and Aurora Lopez de Romo for their unconditional love and persistent stance for me to continue in my education and career. I

thank my siblings and uncle: Aurora, Francisco, Karol Romo and Gabriel Lopez, who have encouraged me the last few years and have given me their strong support in my personal, academic, and professional development.

Table of Contents

List of Figures

1 Introduction

This chapter essentially focuses on the motivation for the present work, and introduces key optical features (i.g. surface plasmon resonance (SPR), excitons, transverse (T) peak, longitudinal (L) peak, and aspect ratios), discrete dipole approximation (DDA) software, and 2D-transition metal dichalcogenides (TMDs) (e.g. WS_2). General details of these three topics and the current research performed with noble metal - noble metal and semiconductor - noble metal will be emphasized and discussed. This chapter ends with an overarching hypothesis and research objective.

1.1 Motivation

1.1.1 Sustainable energy

The world's growing population will demand a supply of affordable, clean energy [1]. The global energy demand is projected to rise from 17 TW in 2010 to 30 TW by 2050, a 176% increase [2]. The primary energy sources are fossil fuels, and they have been the dominant global energy source for years and have produced increasing concerns over the effect of anthropogenic carbon dioxide on the earth's climate [2-4]. In recent years, world leaders have agreed on setting key goals to help reduce the carbon footprint. One of the main goals for reducing the carbon-emission was finding alternative sustainable energies that can support the escalating demand of a growing population and maintain an ecological balance. Sustainable energy technologies, such as wind, solar, and geothermal [5-9] have made significant improvements via plasmonic nanostructure/materials. Specific examples for these improvements include enhancement of electron-hole pairs, i.e., excitons (and photocurrent) in solar photovoltaics [10], and efficient catalytic activity in fuel cells [10-14]. However, critical challenges such as high cost of producing these materials (e.g., electron beam lithography, chemical vapor deposition) have

limited the performance improvement for the plasmonic nanostructures [15,16]. Part of this work has focused on performing an alternative method to mass produce cost-effective noble metal - noble metal (e.g. dimers) and noble metal - semiconductor heterostructures. These inexpensive nanoantennae have been studied experimentally and computationally for their unique enhanced optical features. The produced optical features such as room temperature excitons and surface plasmon resonance at the near infrared region help validate this heterostructure's ability to produce optical emissions for alternative energies.

1.1.2 Medical enhancement (tumor ablations)

Cancer, a significant threat to human life, causes more than eight million deaths yearly [17]. A solution to manage cancer has been a primary focus in medicine. In particular, nanotechnology has demonstrated promise for cancer therapy through noninvasive ablation on diseased tumor cells via light-activated therapies [18,19]. Specifically, gold nanorods (AuNRs) [18], gold nanostars (GNS) [17], and gold nanoparticles (AuNPs) [20-22] show potential with their electromagnetic (EM) and optical properties to ablate malignant cells through plasmonic photothermal therapy (PPTT). Additionally, AuNPs have been successful in immunotherapeutic application, where delivery of immunomodulation materials (e.g., antigens, checkpoint inhibitors, and cytokines) assist with mitigating the cancerous cells [22]. Adequate progress has been performed to mitigate tumors with nanoparticles. However, the manufacturing of these AuNPs uses the toxic cetyltrimethylammonium bromide (CTAB) and silver nitrate growth conditions [18]. These seeded growth conditions result in the surface chemistry of the AuNPs becoming cytotoxic hence hindering the opportunity for nanoparticles to become the leaders in tumor ablations [23]. Citrate-coated gold nanospheres (AuNSs) merged via centripetal force produce a nontoxic nanodimer (noble metal - noble metal) that has the potential to be used as a

PPTT [24]. These overlapping AuNSs have optically demonstrated visible to near infrared region (NIR) features that correspond to the transverse and longitudinal peaks predominantly found in the aspect ratio of AuNRs and prolate nanoparticles (NPs) [25-29]. New distinct features arise in the computational optical spectra of these nanodimers, and an in-depth study for these nanostructures has been performed in this research. These distinguishing features in merged AuNSs have the potential to broaden the medical community use of alternative nontoxic nanostructures for tumor mitigations.

1.2 Background

1.2.1 Plasmonic properties of nanomaterials

Relatively small metal nanostructures such as gold and platinum tend to alter the electromagnetic energy through plasmons [30,31]. Drastic change in the nanostructure's geometry determines the EM energy intensity output as well as the breadth of extinction efficiency optical spectra. As incident light hits the nanostructure the resonant EM energy produces a surface plasmon, a collective oscillation of electrons that is confined within the dielectric interface [32]. A phenomena known as localized surface plasmon resonance (LSPR) happens when the plasmons are confined in the surface of the metallic material. In Figure 1.1, two subwavelength metallic spheres demonstrate the LSPR phenomena where the proper placement of electrons and photons acquired under EM intensity is shown. Under unique conditions, the metallic nanostructures have absorptive behaviors when induced with an incident light that translates to intense electric near-fields. These absorptive behaviors intensify the heat in the surface of the nanostructure. Studies of this phenomena are applied to surface-enhanced Raman spectroscopy (SERS) [33,34] and heating applications (i.e., tumor ablations) [5,35] to optimize the use of nanoantennae. For this work, Au and Pt nanostructures utilize EM waves for

enhanced optical activity, which offers improved potential in optoelectronics [12,37-40] and biomedical treatment applications [17-22].

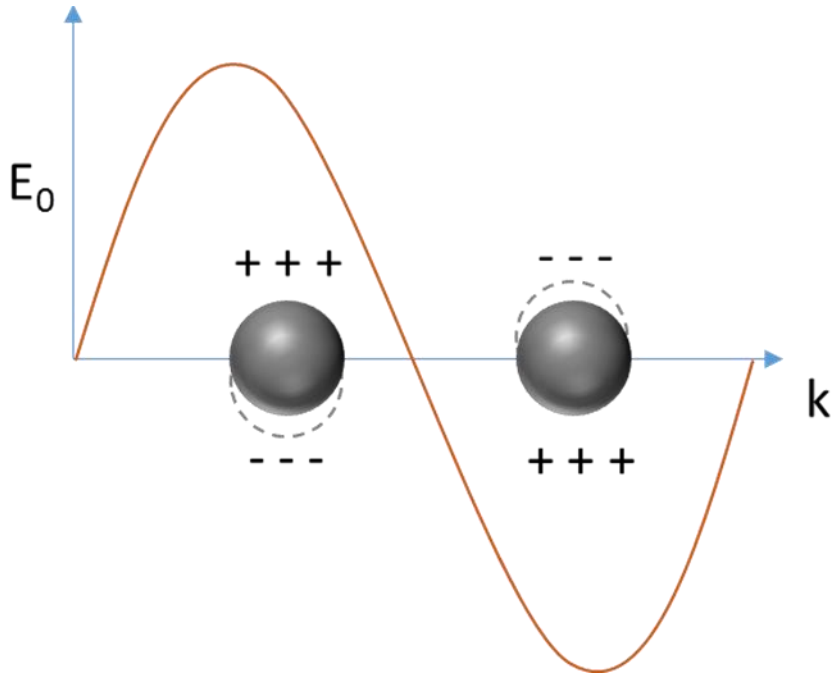

Figure 1.1 Subwavelength metallic sphere with induced dipolar plasmon. E_0 is the amplitude of the electric field and wave vector is k.

As spherical nanostructures extend from their shape to geometric shapes like ovoids and nanorods, the plasmon resonance will split into two modes: longitudinal and transverse. The longitudinal mode is produced from the long axis of the nanostructure, and the transverse mode is due to the perpendicular axis [40]. The rod-like shape of gold nanorods (GNRs) has LSPR plasmons that reach the wavelength range of both visible and NIR [25,41]. The longitudinal wavelength of elongated nanostructures is controlled by the aspect ratio, the ratio of length to width of a nanoparticle, where the higher the aspect ratio the more red shifted the longitudinal wavelength peak [40]. Nanostructures such as overlapping AuNSs have the same characteristics as GNRs. However, these nanostructures are less toxic for they do not require the toxic capping ligand of cetyl trimethyl ammonium bromide (CTAB). An in-depth study of the optical

characteristics via DDA simulations for these dimers will assist in further grasping the ultimate dimensions of nanostructures for tumor ablations and optoelectronics.

1.2.2 Transition metal dichalcogenides

Monolayer transition metal dichalcogenides (TMD) produce room temperature excitons, electron-hole pairs confined through a Columbic force, which result from the direct bandgap within the angstrom scale structure [42]. TMDs are composed of two chalcogen atoms (e.g., sulfur or selenide) coated around a transition metal atom (e.g., tungsten or molybdenum). Multiple TMD monolayers can adhere to one another by Van der Waals bonding, which produces the natural bulk state of the TMD material. The bulk TMD has been studied since the 1960s [44-46] and is currently abundant and low cost. Until the early 2000s, 2D TMDs were not diligently studied for their optical, electronic, and physical properties, but interest rose a few years after graphene was discovered [46]. In recent literature, 2D TMDs are reported to be used for hydrogen and oxygen evolution reaction (HER and OER) systems [10,47,48], and field-effect transistors (FETs) [49]. The 2D TMD, specifically WS_2, exhibits unique optoelectronic and optical activity in the visible (Vis) wavelength range [50]. This optical activity in the Vis range was the main component for the selection of 2D semiconductive material to be combined with noble metal nanoparticles.

The ability to modify and enhance optical activity in the Vis range made TMD monolayers optimal candidates for this research. As previously mentioned, stacks of monolayer WS_2 nanosheets make bulk TMD material which tends to be indirect band gap semiconductors. Indirect band gaps give off optical spectra similar to that of turbid solutions, which have no response in the Vis range. To improve the Vis range response, direct band gaps from WS_2 TMD monolayers would have to be produced. This direct bandgap alters the electronic band structure,

which positions direct transistors at the K point (~ 2 eV, A exciton, 620 nm) of the Brillouin zone [42]. Energies with much higher direct transitions are B (~ 2.38 eV, 520 nm) and C (~ 3 eV, 420 nm) excitons. Monolayer WS_2 TMD crystal structures have two well-known structural polytypes: the octahedral (2H) and the trigonal (1T) coordination [51,52]. With the octahedral phase a natural semiconductive phase can transform to a metallic trigonal phase [53] by electrical and optical stimuli [54]or elemental doping [55].

The production of the 2D WS_2 TMDs involves exfoliating bulk crystals or chemical vapor deposition (CVD) growth. Attaining cost effective macroscale 2D TMD wafer discs have been a driving force in finding high yield exfoliation techniques. Three well defined methods — mechanical [42,49], chemical [55], and liquid [51,56,57] — have been successfully used to exfoliate the TMD bulk material. Mechanical exfoliation uses adhesive tape, similar to graphene production, to easily extract 1-10 μm length scale monolayer TMDs, however, using this method gives low throughput and little or no control of thickness [58,59]. Chemical exfoliation uses an electrochemical cell that requires lithium ions to intercalate between TMD monolayers so that the Van der Waals force can easily weaken [55,60]. The downside of using chemical exfoliation is high temperature (300 °C) required to anneal the 1T metallic phase to the optimal 2H semiconductive phase [55]. This can become costly because the high temperature has to be set for many hours. Liquid exfoliation requires sonicators that provide strong vibrating sound waves to break the Van der Waals force within the bulk TMD [61,62]. This route provides low-cost and high-yield of few layer TMDs that can be scalable for mass production. In this work, two liquid phase exfoliation techniques (probe and freeze-thaw) were implemented on bulk WS_2 in order to acquire low-cost, and scalable colloidal WS_2 nanoflakes that were decorated with noble metals. These noble metals - semiconductors were characterized for their enhanced optical properties.

1.2.3 Discrete Dipole Approximation (DDA)

Computational models such as finite difference time domain (FDTD), boundary/finite element methods (BEM/FEM), T-matrix, and discrete dipole approximation (DDA) are used to model and configure optics of nanoantenna systems to Maxwell's equations [64-67]. The DDA software allows for simple parametrization and the ability to discretize only the particle volume, which makes the nanostructure simulations less time and computationally demanding. BEM, FEA, and FDTD software require complex parametrization, difficult application to arbitrary dielectric functions (ε (ω)), high time consumption, and parametrization of the volume outside the particle compared to DDA [67,68]. The DDA software also provides the ability to move/remove individual dipole points within the geometric shape, while other popular software packages, e.g., BEM and FEA, do not utilize individual dipole points for the simulations. DDA, BEM, and FEA have shown comparable experimental and simulated transverse (T) and longitudinal (L) optical spectra for merged AuNSs and AuNRs with varying computational parameters, e.g., individual dipole points and bulk material properties [42,70-72].

The DDA is a key resource for this work that solves Maxwell's equations for absorption and scattering of electromagnetic waves.. DDA treats nanostructure dimensions as a collection of dipole points in a Cartesian plane. The polarizability, α_i, for each dipole point is calculated by the Lattice Dispersion Relation [66]. The independent variable, local electric field, is correspondent with the dependent variable, polarization magnitude for each target sub-volume($\boldsymbol{P}_i$), and it is determined in eq. 1:

$$\boldsymbol{P}_i = \alpha_i\left(\boldsymbol{E}_{o,i} - \sum_{j\neq i}^{N} \boldsymbol{A}_{ij}\boldsymbol{P}_j\right) \qquad \text{(Equation 1)}$$

where $\boldsymbol{P}$ is the polarization density, $\boldsymbol{E}$ is the electric field, α is the polarizability, and **A** is the dipole-dipole interaction matrix.

The scattering, extinction, and absorption cross sections, σ_{sca}, σ_{ext}, and σ_{abs} , respectively, are determined as:

$$\sigma_{ext} = \frac{4\pi k}{|\mathbf{E}_o|^2} \sum_{j=1}^{N} I\left(\mathbf{E}_{o,j}^{*} \cdot \mathbf{P}_j\right) \quad \text{(Equation 2)}$$

$$\sigma_{abs} = \frac{4\pi k}{|\mathbf{E}_o|^2} \sum_{j=1}^{N} \left\{ I\left[\mathbf{P}_j \cdot \left(\alpha_j^{-1}\right)^{*} \mathbf{P}_j^{*}\right] - \frac{2}{3} k^3 \left|\mathbf{P}_j\right|^2 \right\} \quad \text{(Equation 3)}$$

$$\sigma_{sca} = \sigma_{ext} - \sigma_{abs} \quad \text{(Equation 4)}$$

where I is the intensity and k is the wave vector. This work utilizes DDA to guide design and describe the optical behavior of nanoantennas from the LPE WS_2 nanoflakes decorated with noble metals and two merging gold nanospheres. Having the DDA to perform the near far-field spectra will demonstrate the computational optical features that are enhanced by the heterostructures.

1.3 Key advances of the present work

For this thesis, it is hypothesized that interfacial contact between adjacent nanostructures (i.e., noble metal - noble metal and noble metal - semiconductor) enhances optical activity at UV-Vis-NIR electromagnetic spectrum. This is demonstrated in two subsections where it is shown that: (i) reduction and simulation of noble metal nanoparticles with 2D semiconductor transition metal dichalcogenides can produce a heterostructure nanoantenna for enhanced optical spectra at the UV-Vis region, and (ii) simulated nanostructures of two merged sub-25 nm diameter gold nanospheres produce a heterostructure nanoantennae for enhanced optical spectra at the Vis-NIR region.

This research focused on performing liquid phase exfoliation and a chemical reduction to mass produce a cost-effective noble metal-semiconductor heterostructure. It also focused on analyzing the experimental and computational enhanced optical spectra via spectrometry and

DDA. The produced optical features such as room temperature excitons and surface plasmon resonance at the near infrared region confirmed these heterostructures ability to produce optical emissions for alternative energies and tumor ablations. The primary focus of the research was the fabrication techniques, the development and identification of design consideration, and characterization methods of nanoantennae for UV-Vis-NIR region optical feature enhancements.

The significant advances made in this study were:

1. creations of 2D transition metal dichalcogenides nanoflakes via the probe and freeze and thaw liquid phase exfoliation, then decorating PtNPs on the 2D nanoflake;
2. investigated correspondent optical features from characterized Pt-WS_2 via SEM/TEM and EDS mapping UV-Vis spectra and in silico DDA simulations; and,
3. characterized colloidal merged AuNSs and compared to in silico DDA merged AuNSs for similar optical Vis-NIR region optical features.

2 Pt-WS_2 Heterostructure Nanoantennae

In this chapter, the fabrication of monolayer WS_2 was performed by two liquid phase exfoliation techniques: probe and freeze/thaw sonication. Both methods are relatively cost-effective and produce a significant amount of colloidal WS_2 nanoflakes when compared to the counter techniques of mechanical and chemical exfoliation. These WS_2 nanoflakes were decorated with promising noble metal (platinum) nanoparticles via a reduction technique. Scanning electron microscopy (SEM), transition electron microscopy (TEM), energy-dispersive x-ray spectroscopy, and optical spectroscopy was performed to demonstrate the heterostructure nanoantennae's characteristics. Simulations of a TEM image of the heterostructure nanoantenna was performed via DDA. The results were used to analyze the enhanced optical features for both experimental and computational spectra.

2.1 Exfoliation of bulk WS_2

2.1.1 Freeze and thaw sonication of bulk WS_2

Raw materials used were bulk tungsten disulfide (WS_2) powder, sodium cholate, and degassed deionized water. Six sodium cholate solutions (ranging from 1 - 6 mg/mL mass concentration) were produced by mixing cholate with degassed deionized water. The bulk WS_2 powder was mixed with each sodium cholate solution in a plastic centrifuge tube to attain 30 mL with a concentration of 10 mg/mL. Afterward, all six samples were placed in a freezer at -20 ℃ for at least 90 minutes and then submerged in a sonication bath for 10 minutes. The expansion of the frozen water and the vibrations from the bath sonicator caused the bulk WS_2 to weaken the van der Waals forces, which made the crystal layers separate [78-80]. The samples were then returned to the freezer and the process was repeated for a total of 24 iterations. After the last iteration, all six samples were centrifuged at 372 g for 120 minutes [39]. The supernatant was

then transferred to a cuvette, as shown in the inset of Figure 2.1. In its bulk form, WS_2 will emit a black/gray color. An observable indication that sufficient TMD monolayers were within the solution was the emitted green color from the cuvette. In Figure 2.1, cholate mass concentrations of 4 mg/mL and above demonstrated a strong green tint, indicating that an increase in the surfactant concentration led to an increase in the efficiency of the exfoliation process. The

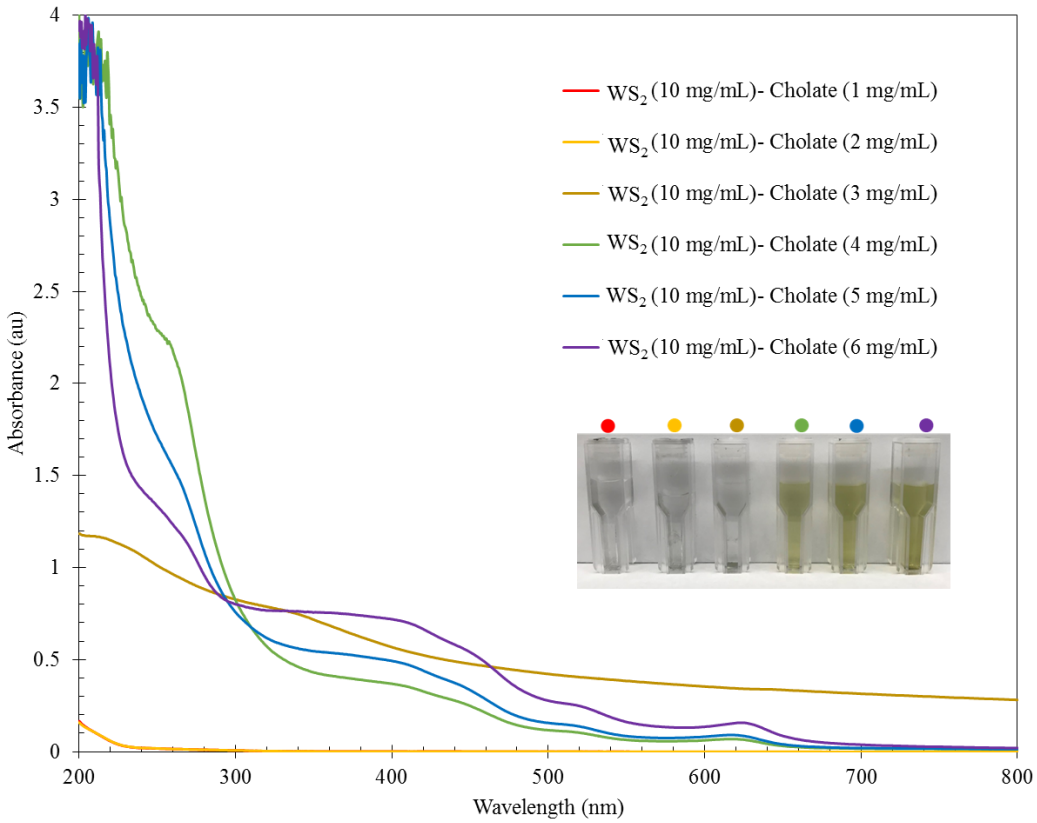

Figure 2.1 Optical spectra for freeze and thaw exfoliated WS_2. The exfoliated WS_2 solutions have a range of 1-6 mg/mL cholate mass concentrations. Inset image: picture of cuvette's with corresponding colored dot to WS_2-Cholate solution. Spectra for WS_2 (10 mg/mL) - cholate (1 mg/mL) (red) is located behind the WS_2 (10 mg/mL) - cholate (2 mg/mL) (yellow).

supernatant in the cuvettes was analyzed using a UV spectrometer which measured the absorbance of light from 200 to 800 nm wavelengths.

The spectra for the respective cuvettes were analyzed and the UV spectra exhibited the presence of A (~620 nm), B (~510 nm), and C (~420 nm) excitons. As previously mentioned, the

unique ability of producing room temperature excitons from monolayer TMDs provides a promising semiconductor candidate to decorate with noble metals for optoelectronic and catalytic experiments. The 6 mg/mL solution showed a higher absorbance when compared to the rest of the cholate mass concentrations. The 3 mg/mL cholate sample revealed a diagonal line without indication of excitons, suggesting that there was still some bulk material in the solution. From all of the cholate solutions in the trial, the 6 mg/mL cholate solution showed the highest absorbance with well-defined exciton peaks.

2.1.2 Probe sonication exfoliation of bulk WS_2

Alternatively, bulk WS_2 powder was mixed with a mass concentration of 25 mg/mL into cholate (6 mg/mL). The mixed solution was sonicated in an ice-water bath at 360 W (60% amplitude) in a metal beaker using a probe sonicator with a flat head tip. It was then sonicated for a total of 10 hours with a 6 seconds on, 2 seconds off cycle. Following the long sonication, the unexfoliated WS_2 was removed by centrifuging the solution at 460 g for 90 minutes [39,61]. The supernatant from this centrifugation step was then used to take the spectra shown in Figure 2.2. Also, a 5-hour probe sonication cycle was performed with the same parameters for the probe sonicator. Spectra from the two purchased LPE samples of WS_2 pristine nanoflake solution [Tungsten Disulfide (WS_2), Graphene Supermarket, Calverton, NY] and from the collaborative WS_2 solution from Dr. Jeremy Dunklin at National Renewable Energy Laboratory (NREL) are demonstrated in Figure 2.2 for reference. The dilution ratios (WS_2 solution: WS_2+DI water) for each WS_2 solution are given in the legend. These ratios were configured to attain an absorbance below 3, for 99.9% of the light is attenuated at or above this boundary. All four WS_2 solutions have demonstrated the excitons corresponding to the WS_2 monolayers. For this research, between the two probe sonicated WS_2 solutions, Probe 5 hours was the promising candidate to

attain more WS_2 nanoflakes due to less time and energy spent in exfoliating the bulk material.

Both LPE techniques of the probe and freeze and thaw sonication gave sufficient WS_2 solution to reduce noble metal nanoparticles. Due to its abundance (~ 60 mL) and less time to produce when compared to the alternative LPE technique, the probe sonicated WS_2 solution was selected to be decorated with noble metal nanoparticles.

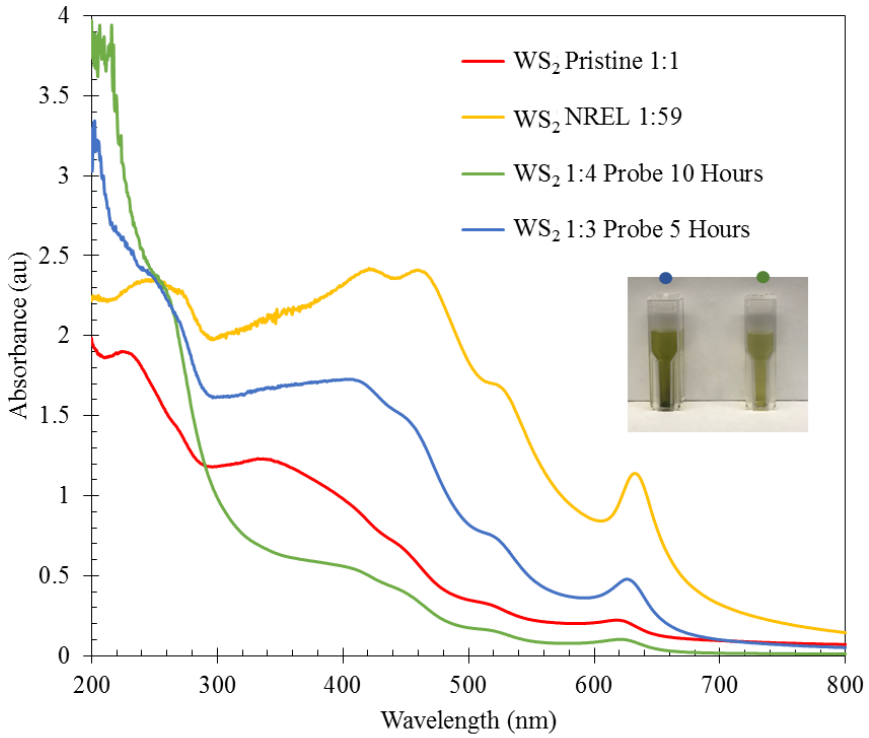

Figure 2.2 Optical spectra for probe sonicated WS_2. Four WS_2 solutions were plotted for comparison. Two were purchased: WS_2 pristine nanoflake solution (WS_2 Pristine) and duplicated 10 hour WS_2 solution from Dr. Jeremy Dunklin (WS_2 NREL). Two were produced in the lab:10 hour probe sonicated WS_2 (WS_2 Probe 10 Hours) , and 5 hour probe sonicated WS_2 (WS_2 Probe 5 Hours). These four samples were diluted to attain absorbance below 3.

2.2 Reduction of platinum nanoparticles onto WS_2 nanoflakes

WS_2 nanoflakes were obtained by the probe sonicated bulk TMD method that had been demonstrated above [39]. It had the most TMD nanoflake solution (~60 mL) when compared to the (~25 mL) freeze-thaw solution, and it also consumed less time (10 hrs vs. 40 hrs). This liquid

exfoliation process yields semiconducting 2H WS_2. The 2H phase exhibits unique optoelectronic properties in the visible region that could support light-induced HER enhancement [39,55]. Sonication in liquid phase exfoliation is reported to increase defect density in the nanosheet [75]. Liquid phase exfoliation of few- to mono-layer 2H WS_2 nanoflakes is scalable, economic, and free from toxic chemicals. This exfoliation contrasts with chemical exfoliation of 1T WS_2 nanosheets via intercalation by lithium. Lithium is reported to adversely affect neuro-transmission, neuropeptide systems, signal transduction pathways, and gene expression *in vivo* [76].

PtNPs were reduced onto liquid-exfoliated WS_2 nanoflakes suspended in aqueous sodium cholate by adding potassium tetrachloroplatinate (K_2PtCl_4) and sodium citrate tribasic dihydrate ($C_6H_5Na_3O_7 \cdot 2H_2O$). Citrate reportedly acts as a reducing and stabilizing agent in depositing PtNPs on nanosheets of graphene [78-81] and TMD [81,82]. In the mixture with K_2PtCl_4 and $C_6H_5Na_3O_7 \cdot 2H_2O$, WS_2 nanoflakes provided a substrate for electroless metal deposition. Substrate catalyzed metallization is widely used to deposit microelectronic vias and to decorate ceramic oxide and polymer with metal island films [84-86]. Figure 2.3 is a schematic of the electrochemical reduction of PtNP on semiconducting few- to mono-layer WS_2 nanoflakes. The present work used citrate and platinum salt concentrations 30-fold higher than those reported by Huang et al. to deposit Pt on lithium-intercalated 1T MoS_2 based on an ostensible 50% MoS_2 recovery from centrifugation [81].

The reduction was conducted in ambient light in the absence, i.e., Pt-WS_2(NL), or presence, i.e., Pt-WS_2(L), of a 150 W halogen lamp. Reduction in ambient light with no halogen lamp yielded Pt-WS_2 adduct consisting of WS_2 nanoflakes approximately 34 nm x 27 nm onto which 1-5 nm diameter PtNPs and larger aggregates were deposited. In contrast, the

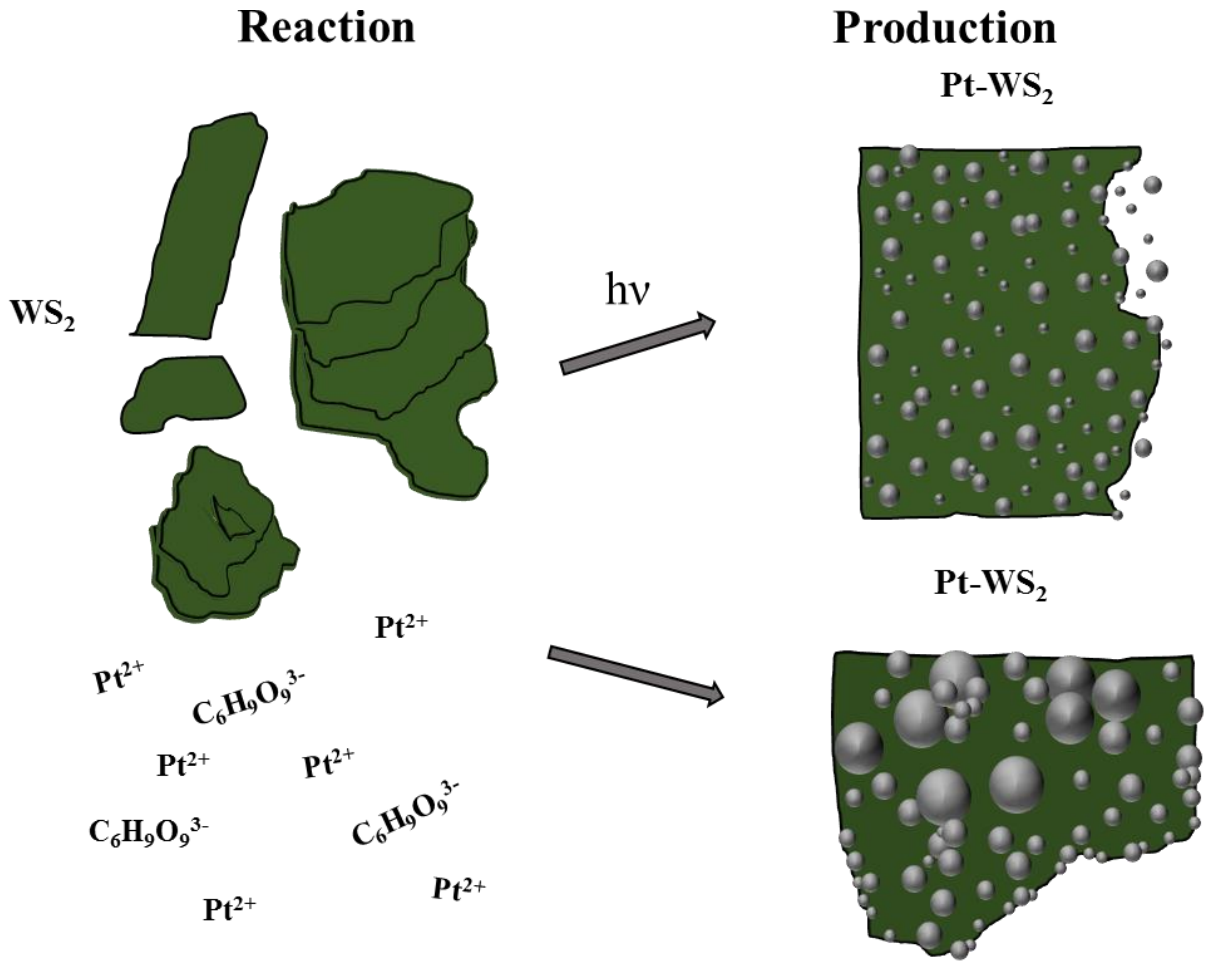

Figure 2.3 Schematic of electrochemical reduction of PtNPs onto WS_2 nanoflakes. An aqueous sodium cholate suspension of size-selected WS_2 nanosheet (upper left) was mixed with potassium tetrachloroplatinate (K_2PtCl_4) and sodium citrate tribasic dihydrate ($C_6H_5Na_3O_7 \cdot 2H_2O$). Subsequent irradiation with a 150 W halogen lamp yielded Pt-WS_2 adduct consisting of WS_2 nanoflakes (ca. 36 nm x 50 nm) with 1-3 nm PtNPs uniformly dispersed (upper right). Reduction in ambient light with no halogen lamp yielded Pt-WS_2 adduct consisting of WS_2 nanoflakes (ca. 34 nm x 27 nm) with 1-5 nm PtNPs and larger aggregates (lower right).

photochemical reduction under the halogen lamp yielded Pt-WS_2 adduct consisting of WS_2 nanoflakes approximately 36 nm x 50 nm onto which 1-3 nm diameter PtNPs were uniformly dispersed. Mean diameter of 2.05 nm (N = 15) calculated for photochemically reduced PtNP was within 0.2 nm of the PtNP diameter recently reported to optimize specific mass activity [86]. Power incident onto the quartz cuvette containing the sample from the overhead lamp is demonstrated in Figure 2.4. Here the surface areas A_1 and A_2 were determined from a halogen

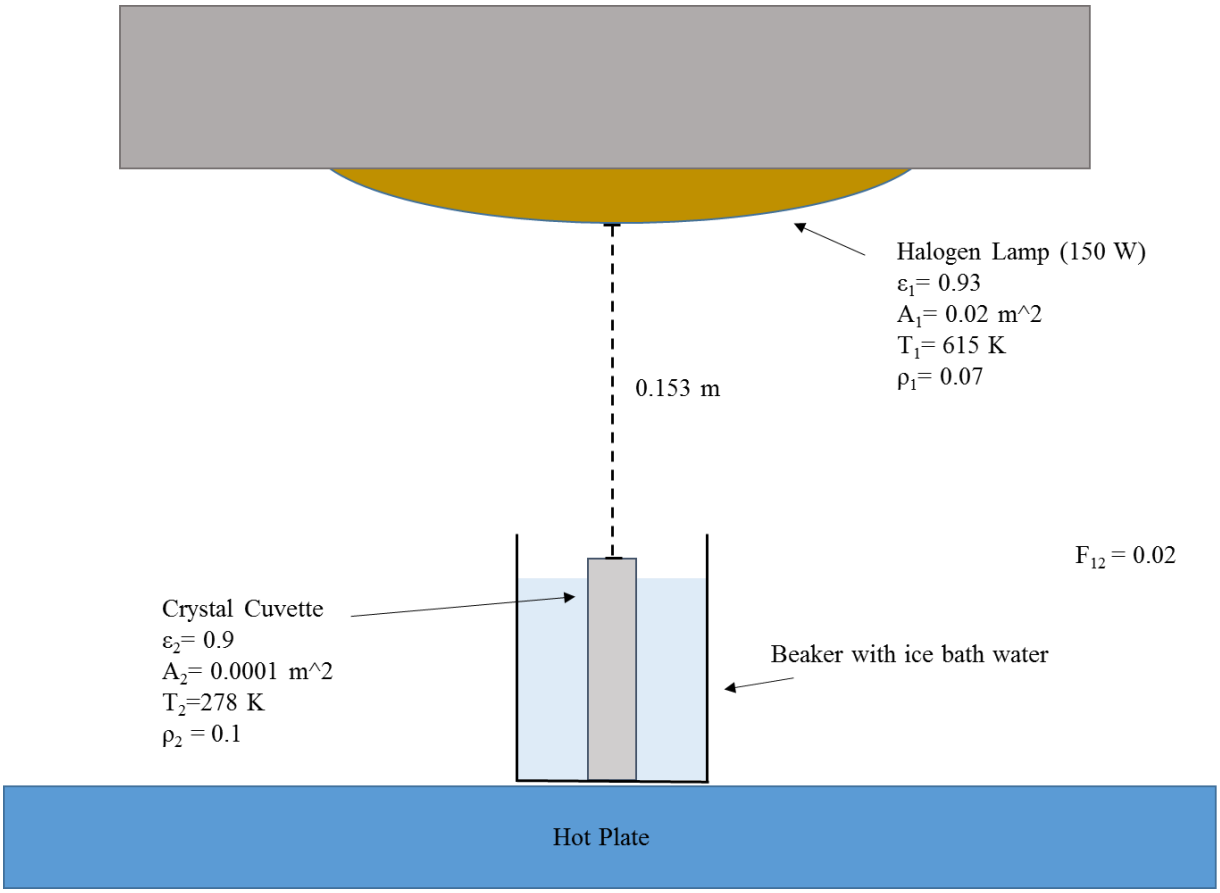

Figure 2.4 Schematic of experimental set-up of the halogen lamp above quartz crystal cuvette. The crystal cuvette contained the reducing Pt-WS_2 (L) solution.

light bulb radius of 0.08 m and the 0.01 m width of the cuvette (square axial projection of 0.01 m x 0.01 m), respectively. Temperatures for both gray surfaces were measured using a thermocouple (Portable Thermometer RDXL4SD, Omega, Norwalk, CT). Average measured temperatures were 613.9 K for the halogen lamp, and 278 K for the cuvette. Values of emissivity and reflectivity for quartz glass material (for the halogen lamp) and water (for the Pt-WS_2 (L) solution) were used [87]. The view factor, F_{12}, was determined based on radiant heat transmission [88] between the two gray body surfaces, which gave a value of ~0.02. The desired radiative heat energy (q_{12}) was calculated using: 5.67 x 10^{-8} (W/m^2*K^4) for the Stephan-Boltzmann constant, σ, T_1 as temperature (Kelvin) for halogen lamp, T_2 as temperature (Kelvin)

for cuvette, reflectivity for both surfaces ρ_1 and ρ_2, surface area for each respective gray body A_1 and A_2, and the view factor F_{12}. The quantitative inputs are demonstrated in Figure 2.4 and placed in Eq. 5.

$$q_{12} = \frac{\sigma(T_1^4 - T_2^4)}{\frac{\rho_1}{A_1 * \varepsilon_1} + \frac{1}{A_1 * F_{12}} + \frac{\rho_2}{A_2 * \varepsilon_2}} \qquad \text{(Equation 5)}$$

The energy incident on the quartz cuvette had a calculated value of 2.134 W.

2.3 Experimental characterization of heterostructure

Morphology and composition of Pt-WS_2 adducts were evaluated with energy-dispersive x-ray via scanning electron microscopy (SEM-EDX) and transmission electron microscopy (TEM) (Figure 2.5). Comprehensive SEM-EDX elemental mapping for Pt-WS_2(L) (pink/yellow/orange) on 20 nm thick SiO_2 TEM grid membrane (teal) is shown in Figure 2.5A. Specific elemental mapping confirmed atomic platinum (Figure 2.5B), tungsten (Figure 2.5C) and sulfur (Figure 2.5D) comprised the surface structures on reacted WS_2 nanoflakes.

Differential absorption by these elements in TEM images (Figure 2.6) indicated PtNPs were deposited on both basal plane and edges of the WS_2 flakes. In contrast, addition of gold (III) chloride to a suspension of liquid exfoliated WS_2 nanoflakes was reported to reduce AuNP directly to uncoordinated edge sulfurs of WS_2 by an Au-S covalent bond [39]. Figure 2.6A-2.6D shows a photochemical reduction of Pt salt under a 150 W halogen lamp onto 2H WS_2 nanoflakes yielded evenly-sized PtNPs with a mean diameter of 2.05 nm (N = 15) distributed uniformly across the nanoflake. Zoom in TEM images and corresponding measured diameters are represented in Figure 2.6C and 2.6D. In contrast, Figure 2.6E-2.6H shows that a reduction in ambient light produced heterogeneously sized PtNPs with a mean diameter of 3.84 nm (N = 15)

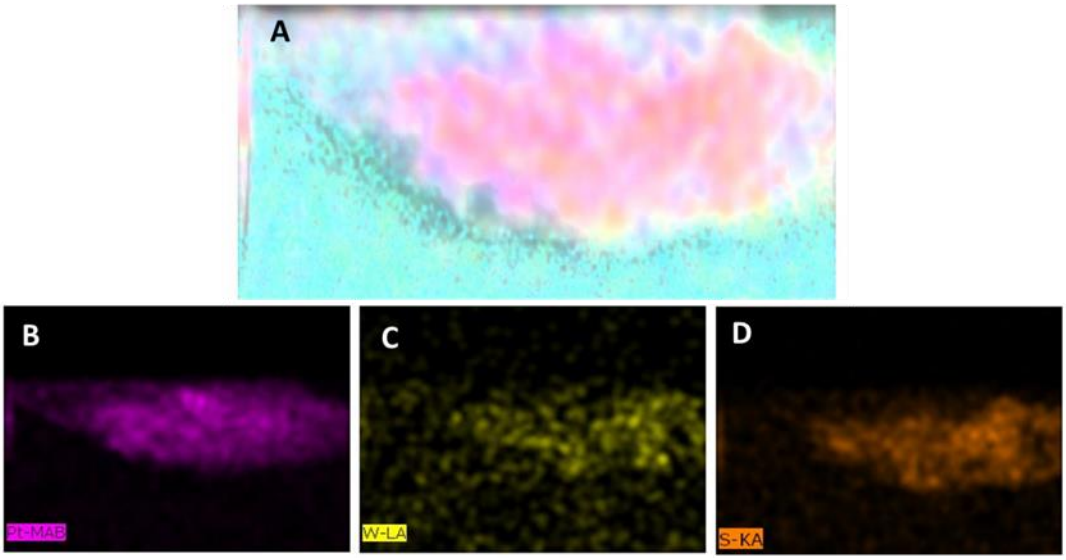

Figure 2.5 EDX imaging of elemental composition for Pt-WS2 heterostructure. SEM-EDX imaging confirmed elemental composition of WS_2 nanoflakes decorated with PtNPs. A) Comprehensive SEM-EDX elemental mapping is shown for Pt-WS_2(L) (pink/yellow/orange) on 20 nm thick SiO_2 TEM grid membrane (teal). Element-specific mapping is shown for B) platinum, C) tungsten, and D) sulfur.

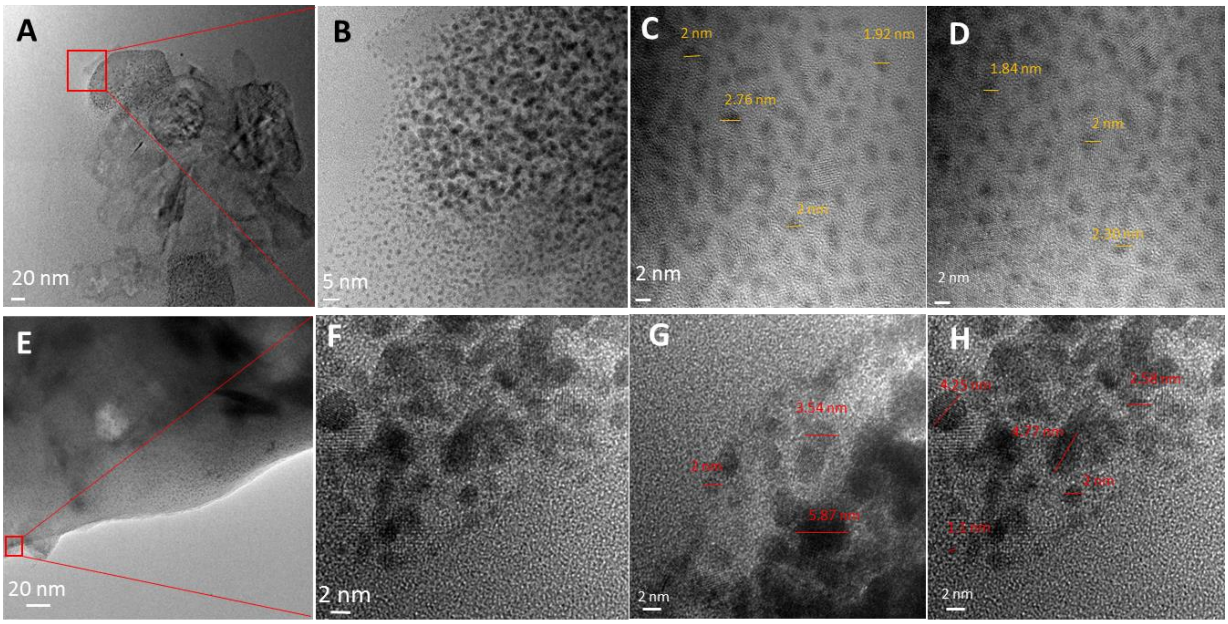

Figure 2.6 TEM images for Pt-WS_2 heterostructures. The photochemical reduction yielded smaller, more evenly-sized PtNPs distributed uniformly across the WS_2 nanoflake. Images shown are for A-D) Pt-WS_2 (L) and E-H) Pt-WS_2 (NL). Individual PtNPs on each WS_2 nanoflake were sized; representative examples are labeled in each image.

and a small proportion of PtNPs with 6 nm diameter distributed unevenly across the nanoflake.

Figure 2.7 shows optical spectra for PtNPs, WS_2, and Pt-WS_2. These three solutions were performed on a NanoDrop 2000c Spectrophotometer (Marshall Scientific, Hampton, NH), which allowed the optical spectra to be read in the UV region. Figure 2.8 shows that spectra in the UV range exhibit optoelectronic activity consistent between PtNPs and Pt-WS_2. It also demonstrates the corresponding A (~620 nm), B (~510 nm), and C (~420 nm) excitons for both WS_2 and Pt-WS_2 solutions. The Pt-WS_2 shows a combination for both noble metal and semiconductor optical activities.

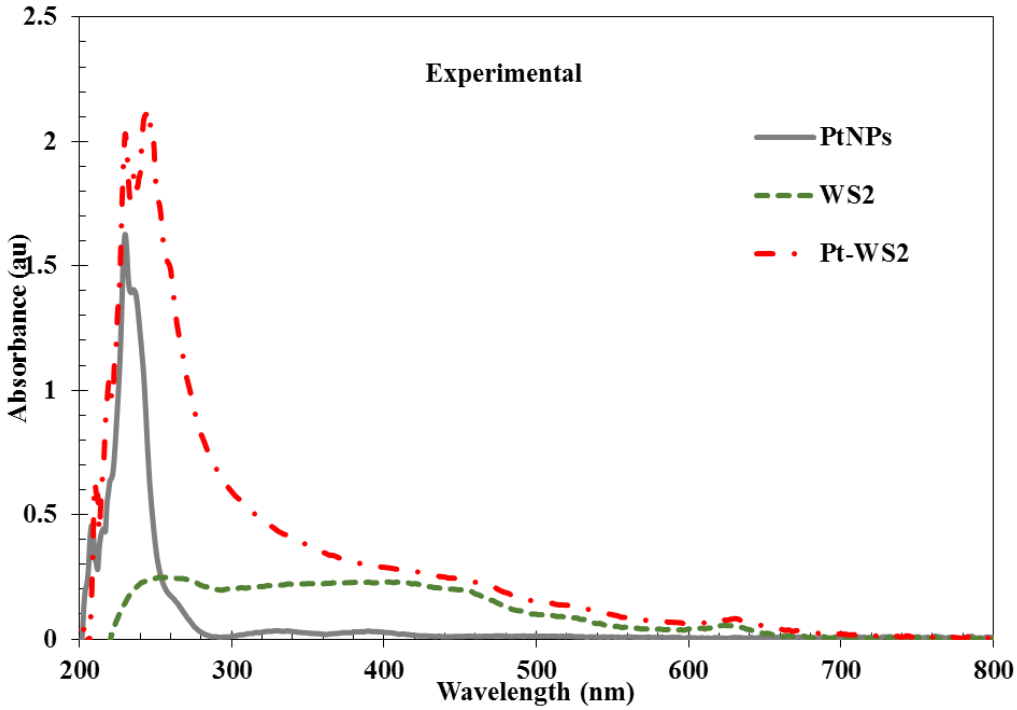

Figure 2.7 Optical spectra for PtNPs, WS2, and Pt-WS_2 nanostructures. The ultraviolet region, 200 nm - 300 nm, had a consistent and dominant absorbance appears for PtNPs and Pt-WS_2 at 228 nm and 247 nm, respectively.

2.4 DDA of PtNPs reduced onto WS_2 nanoflake.

Depositing a PtNP on edge and basal planes of a WS_2 nanoflake enhances its optoelectronic activity. In Figure 2.8, the measured A-exciton peak height at 630 nm (614 nm in

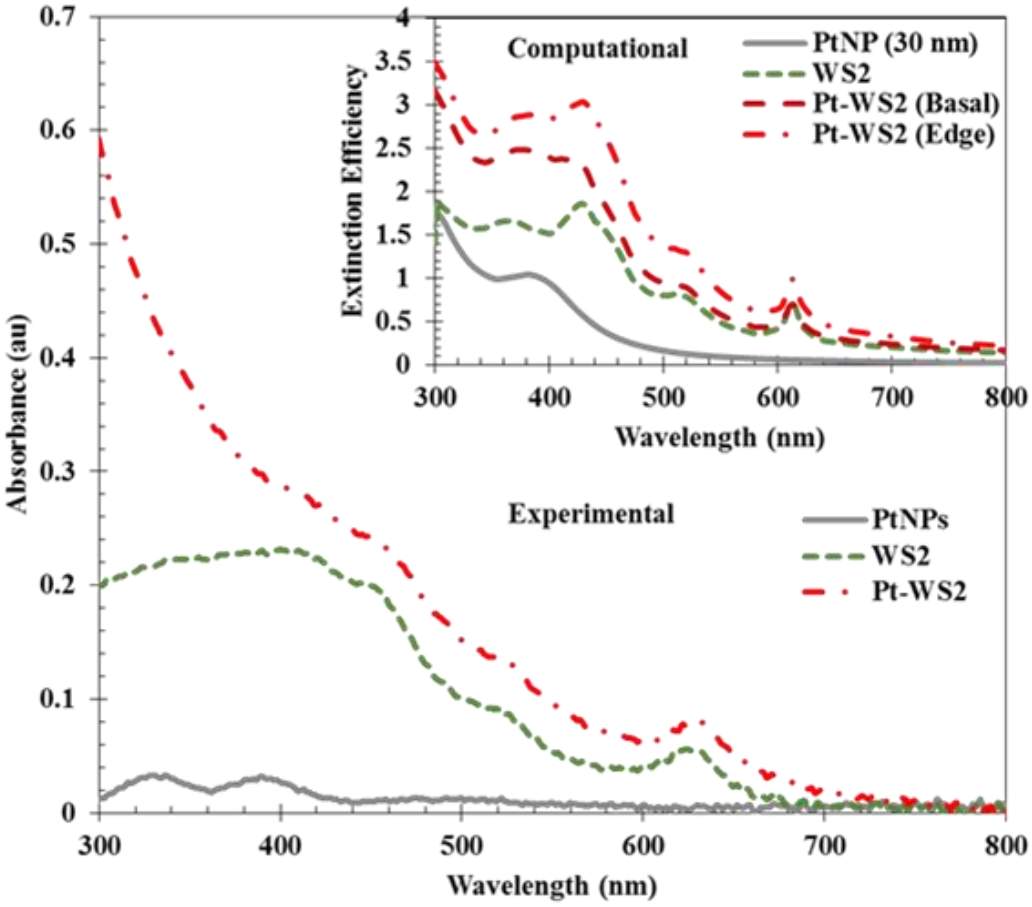

Figure 2.8 Experimental and computational spectra of PtNPs, WS_2, and Pt-WS_2 nanostructures. Inset is corresponding discrete dipole approximation (DDA) spectra for PtNP (15 nm radius), WS_2 nanosheet (50 nm x 75 nm), and basal- and edge-decorated Pt-WS_2 adduct.

simulation) for the Pt-WS_2 adduct increased 1.165-fold from a value of 0.0349 A.U. for neat WS_2 (measured relative to a tangent baseline). Measured B- and C-exciton peaks increased similarly; the average optical absorption from 420 nm to 700 nm increased 0.005 A.U. for Pt-WS_2 relative to WS_2 as a result of adding PtNPs. Simulated spectra in the inset show comparable enhancement of WS_2 exciton absorption due to adjacent PtNP. Observable enhancements at A, B, and C exciton wavelengths occurred due to the edge- and basal-decoration with 15-nm radius PtNP. DDA discretization of 1 nm necessitated the use of a 15 nm PtNP rather than a 2 nm PtNP to obtain simulated spectra and enhanced near field maps. Basal simulation situated the PtNP at

the top center of a 50 nm x 75 nm WS_2 monolayer; edge simulation centered the PtNP at the elongated edge. Simulated peak A-exciton of edge-decorated Pt-WS_2 was 1.42- and 1.43-fold higher, respectively, than basal-decorated or undecorated WS_2.

Discrete dipole simulation maps showed enhanced optoelectronic activity, i.e., extinction efficiency accrues from increased electric field intensity due to irradiated PtNP interacting with edge and basal planes of a WS_2 nanoflake, particularly at resonant exciton frequencies. Local near-field intensities are mapped in Figure 2.9 at incident energies corresponding to the PtNP absorbance as well as the A, B, and C exciton energies. The magnitude of the electric near field increase up to 5-fold at the interface of the PtNP and 2H WS_2 nanoflake. The area of enhancement in the PtNP-decorated nanoflake was significantly larger than the neat WS_2.

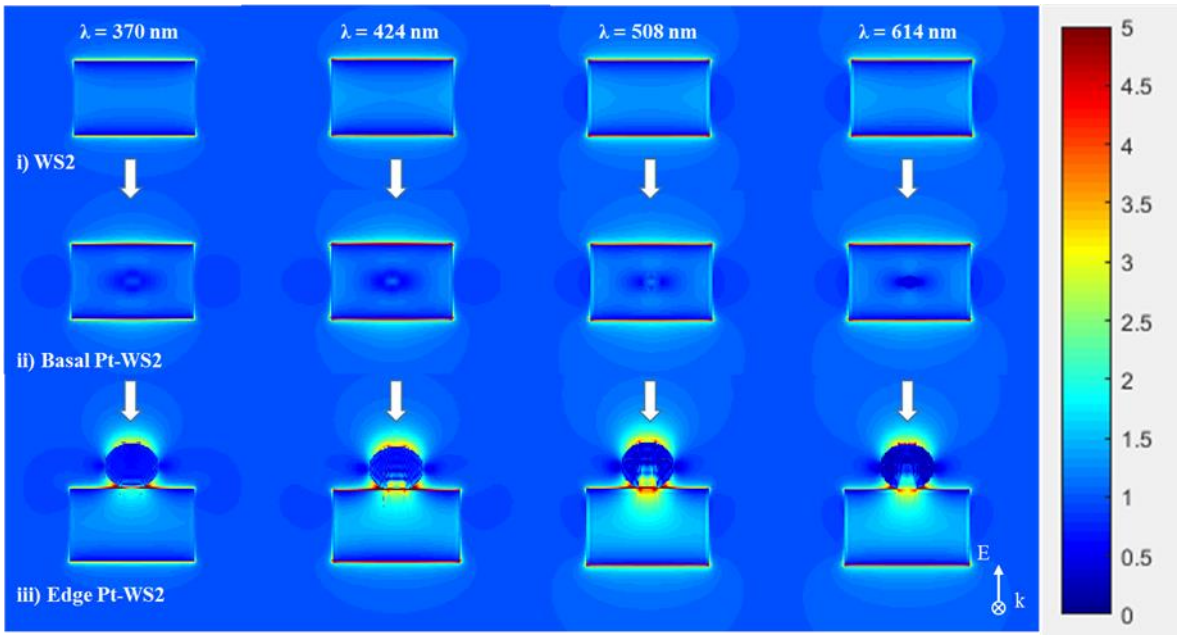

Figure 2.9 Enhanced electric near-field maps at four distinct energies. The four enhanced electric energies are: platinum nanoparticle absorbance (370 nm), and the C (424 nm), B (508 nm), and A excitons (614 nm). These near-field maps show the location of the PtNP as the determinant factor for the electromagnetic (EM) intensity. The edge Pt-WS_2 has the highest EM intensity of all four wavelengths, with the maximum intensity corresponding to the junction point of the noble metal and semiconductor nanocrystal.

2.5 Summary

Comparing simulated and empirical results indicated that the decrease in average PtNP size with more uniform distribution observed in the presence of halogen irradiation could be attributable to the photoelectric effect. In ambient light, PtNP deposition largely proceeded via redox reaction whereby Pt(II) ions were reduced to Pt(0) and either deposited directly on WS_2 nanoflake surfaces or aggregated with adjacent PtNP deposits to form more massive clusters.[89] Under the halogen lamp, redox reaction was complemented by the photoelectric effect in which WS_2 nanoflakes absorbed photons to form electron-hole pairs.[90] Long-lived WS_2 excitons were likely to seed the formation of more PtNPs and accelerate direct Pt reduction onto WS_2 nanosheet surfaces, thereby reducing the availability of dissolved Pt ions, the size of suspended PtNPs, and their propensity to aggregate into clusters up to 6 nm in diameter. Additionally, simulations indicate small PtNPs decorated homogenously at the basal and edge of the semiconducting nanosheet enhances the extinction efficiency. These enhanced optical activities can improve experimental co-catalysts for HER as well as the efficiency for solar cells due to the increased pathway of electrons in the nanostructure.

2.6 Experimental and simulation preparations

Freeze-Thaw-Sonication Exfoliation of TMD

For 30 mL volume, 300 mg of bulk tungsten disulfide, WS_2 (24369-50G; Sigma Aldrich, St. Louis, MO), was added in 30 mL of cholate (C1254-100G; Sigma Aldrich, St. Louis, MO) mixed with degassed deionized water solution resulting in a dark gray suspension. The mass concentrations of bulk WS_2 and cholate were varied with arrangements of 1-6 mg/mL of cholate concentration. The six solutions of bulk WS_2-cholate from 1-6 mg/mL cholate concentration were placed in 50 mL plastic centrifuge tubes (525-0402; VWR, Radnor, PA). All temporary

solutions of plastic centrifuge tubes were implanted into styrofoam which secured and allowed the solution tubes to be submerged approximately 1 cm underneath the bath sonicator's water level. The centrifuge tubes were bath sonicated (Branson 2210R-MT Ultrasonic, Marshall Scientific, Hampton, NH) (Power: 210 W) for 10 minutes at room temperature of approximately 21.6 °C. Subsequently, the solutions were placed in a freezer (Puffer Hubbard) set at -20 °C. They were left in the freezer's racks for 1 hr 50 min ± 10 min. After the freezing periods, the suspensions were again placed in the bath sonicator for 10 minutes. This freeze and thaw process was repeated for 24 iterations. The unexfoliated WS_2 was removed by centrifugation (ModelJ2-21M, Beckman, Brea, CA) at 400 g for 2 hours. The supernatant from this centrifugation was then used to take optical spectra.

Probe Sonication Exfoliation of TMD

Bulk WS_2 powder was incorporated at a mass concentration of 25 mg/mL into a cholate and degassed deionized water mixture of 6 mg/mL. The mixed solution was sonicated in an ice-water bath at 360 W (60% amplitude) in a metal beaker using a probe sonicator with a flat-head tip (942098; JoyFay International LLC, Cleveland, OH). It was then sonicated for 80 minutes with 6 seconds on, 2 seconds off cycle. Following this sonication, the dispersion was centrifuged (913023419999; Scilogex, Rocky Hill, CT, USA) for 1.5 hours at 1700 g. Afterward, the supernatant was removed and discarded. The precipitate was then re-dispersed in 75 mL of 2 mg/mL aqueous cholate solution. Subsequently, the WS_2 dispersion was sonicated for 10 hours at 360 W (60% amplitude) in a metal beaker using the same flat-head tip probe sonicator with 6 seconds on, 2 seconds off cycle. Ice was added to the ice bath every 2 hours; this was done to ensure aggregation-inducing heat was mitigated. Following sonication, the unexfoliated WS_2 was removed by centrifugation at 460 g for 90 minutes. The supernatant from this centrifugation was

then used to obtain the spectra. For the 5-hour probe sonication, everything was performed the same except a sonication time of 5 hours was used instead of 10 hours.

UV-Spectra

Probe and FT optical sonication extinction were taken via UV-probe (UV-1800 UV-Vis Spectrophotometer, Shimadzu, Kyoto, Japan) with two crystal glass cuvettes (CV10Q3500, Thorlabs, Austin, TX). The samples were diluted accordingly, where the first cuvette was filled with 2 mL of the respective solution, and the second cuvette was filled with 2 mL of deionized water. Optical extinction was measured using transmission UV-vis-NIR spectrometry. For spectral analysis, Pt-WS_2 (L) solution was diluted at a 1:2 ratio to yield 1.204 and 0.0927 mg/mL concentrations of platinum and WS_2, respectively. In situ reduced PtNPs were diluted 1:3 to obtain 1.204 mg/mL platinum. Liquid-exfoliated WS_2 suspension was diluted 1:43 based on the spectroscopic determination of its concentration to obtain 0.0927 mg/mL concentration.

Reduction of Pt onto WS_2

About 18 mg (± 1.5 mg) of potassium tetrachloroplatinate (II) (K_2PtCl_4) powder (Sigma-Aldrich, St. Louis, MO) and 20 mg (± 2.0 mg) of sodium citrate tribasic dihydrate ($C_6H_5Na_3O_7 \cdot 2H_2O$) powder (Sigma-Aldrich, St. Louis, MO) were combined in a crystal cuvette. Deionized water was added to the cuvette to prepare a total volume of 3 mL, and the solution was mixed at 900 rpm using a magnetic stirrer. While stirring, 167 µL of a 3.9 mg/mL dispersion of liquid exfoliated WS_2 nanoflakes was added to the solution to activate reduction. The cuvette was placed in an ice bath and irradiated with a halogen lamp (150 W). The temperature was monitored in order to ensure that the solution remained under 20 °C. The solution was allowed to react for two hours. Following this, centrifugation was performed at 8500 rpm for 20 minutes, and the supernatant was extracted in order to remove unreduced material. This reduction

procedure was repeated to produce an additional sample that was allowed to react without the use of the halogen lamp.

TEM, SEM, and EDX

TEM, SEM, and EDX spectroscopic analyses were performed at the University of Arkansas Nano-Bio Materials Characterization Facility. SEM and EDX spectroscopic analyses of the samples were made using an FEI Quanta 200 instrument operating at 30.0 kV. TEM was performed on a Cs-corrected FEI Titan 80-300 (FEI, Hillsboro, OR). Sample volumes of 1.5 µL, corresponding to Pt-WS_2 reduced with and without halogen lamp irradiation, were drop-casted onto 20 nm thick SiO_2 membranes (SPI Supplies, West Chester, PA). TEM grids were preheated to 105 ± 5 °C to flash evaporate the solvent for minimal aggregation.

Simulation characterization

Simulations from 300 to 800 nm wavelengths were performed on a 16-core supercomputer node with 64 GB memory. Refractive index of water (1.33) was used. The limit of the resolution was 1 nm. Target and parameter files for DDSCAT v7.3 were developed with a custom MATLAB tool available on nanoHUB [91]. PtNP of 15 nm radius and WS_2 rectangular prism of 50 nm x 75 nm area were discretized according to Cartesian descriptions with the dielectric functions from A. Rakic et al.[92] and Y. Li et al.[93], respectively. The enhanced electric near-field maps had the field set to 1.33 with 1 nm resolution. Each near-field simulation was performed at the A, B, C-exciton and platinum nanoparticle absorbance wavelength (614, 508, 424, and 370 nm).

3 Noble Metal - Noble Metal Nanoantennae

In this chapter, optical responses of variations in the geometry between overlapping AuNSs showed precision for the simulations to attain dimer geometries used for similar optical spectra for colloidal AuNSs. Characterizing the dimers involved repopulating and unpopulating dipole points at the cleft region of two merging sub-25 nm AuNSs. DDA was used to characterize these dimers. Extinction spectra from DDA demonstrated a trend of red to blue shift at the longitudinal peak as the overlapping distance of merged AuNSs incremented. The spectra also showed unpredicted multi plasmon resonance (multimodal) features for sharp cleft depth dimers when compared to shallow cleft depth dimers. From the unique NIR multimodal features, Microsoft Excel was used to combine the individual dimer spectra to corresponding similar spectra for colloidal merged AuNSs. Error differences below 2% were attained from combined characterized dimer spectra and colloidal AuNSs. Subsequently, two dipole points were adjusted symmetric (180°) and asymmetric (90°) at the cleft region, which caused a red and blue shift at the 850 nm wavelength peak. These new and unique modifications in the interparticle junction area (cleft region) can assist dimers with application in optoelectronics and biomedical treatments by using the high electromagnetic (EM) intensity as a fountain of energy for other nonmetallic dielectric material.

3.1 Geometric dependence on NIR multimodal activity of simulated dimers

In this work, two AuNSs were merged 1 nm (distance between two dipole points) at a time, which formed a cleft region between the two spheres. The geometric distinctions on the dimers resulted in the development of multimodal features in the NIR region of the optical spectra as demonstrated in Figures 3.1-3.4. The two AuNSs were generated using dipole points in DDA software, which utilizes Maxwell’s equations to extract extinction, scattering, and

absorption efficiencies. DDA has been used for a variety of geometric shapes, e.g., NSs and NRs, that resulted in comparable experimental and computational optical properties [36,94,95]. Chen et al. used a sintering technique to merge two 4.8 nm AuNSs to show that the Au was malleable and resulted in a curved cleft interface rather than a sharp cleft interface observed with bulk Au [96]. In this work, dipole points were moved to replicate this curved interface structure (repopulated) or were removed to show the resulting optical properties for sharp cleft structures (unpopulated). The DDA software provides the ability to move/remove individual dipole points within the geometric shape, while other popular software packages, e.g., BEM and FEA, do not utilize individual dipole points for the simulations. Relative to BEM and FEA, DDA software reduces the complexity of generating the dimer and the computational demand for outputting the optical properties for the simulated dimers. These improved factors allow dipole approximation methods to require less computing power and time when compared to BEM and FEA. DDA, BEM, and FEA have shown comparable experimental and simulated transverse (T) and longitudinal (L) optical spectra for merged AuNSs and AuNRs with varying computational parameters, e.g., individual dipole points and bulk material properties [69,70,97].

The merging of two AuNSs resulted in the formation of multiple optical features in the NIR from the various aspect ratios of the L peaks with the maximum L peak red-shifting as the cleft depth between the AuNSs increased, and blue-shifting as cleft depth decreased as the AuNSs were merged further. Figures 3.1-3.4 show the extinction efficiencies for a single AuNS (7, 7.5, 8, and 24 nm radius). Regarding the AuNS with 7 nm radius (Figure 3.1), a single optical feature was observed with a peak extinction efficiency of ~ 0.9 for the LSPR (T peak at 532 nm) while two AuNSs with a 1 nm gap between them resulted in a higher extinction efficiency (~1.25) and a slight red-shift (547 nm) in the optical feature. As these two AuNSs were merged

at 1 nm intervals and dipole points were moved/removed, multiple optical features were observed as the T and L peaks were both impacted by the merging as a result of the varying aspect ratios. The maximum L peak was observed to redshift with increasing cleft depth for both unpopulated (pair 4) and repopulated (pair 3) dimers (Figure 3.1). Sheikholeslmi et al. demonstrated similar multimodal peaks at the NIR and called them DDA artifact[41]. A small number of dipole points (<5000) is a probable cause for this low-resolution outcome of spectra and these 14 nm Au dimer simulations had approximately 2800 dipole points. However, additional simulations of larger AuNP diameters (24 nm) shown in Figure 3.4 have increased the number of dipole points to well over 5000 yet still produced similar optical features in the NIR region. Similar multipole optical features were observed in elongated annulated gold disks (90 x 60 nm) where computational EELS spectra accounted for the major peaks to be bright bonding modes [98]. These bright modes are strong indications of charge interaction between adjacent surfaces along the inner and outer edges of the Au nanodisks. Strong charge interactions between adjacent surfaces, in this case, the cleft region, become accountable for a small portion of the multiple optical features (multiple LSP resonances) in the NIR region. The outer surrounding area of the dimer heterostructure provides a strong correlation to the multi bright modes.

As the cleft depth began to decrease when the AuNSs were merged further, the maximum L peak was observed to blue shift. This blue-shifting as the two AuNSs overlapped during the merging was previously reported by Romero et al. for two merging AuNSs with 60 nm radii [71]. The cleft depth and overlapping distance (d) for the dimers were divided by the AuNS radius (a) to obtain calculable ratios for each dimer [71]. In Figure 3.1 (a), as the d/a ratio decreased from 0.0 (pair 1) to -0.428 (pair 4), the maximum L peak red-shifted and the total number of optical features in the NIR increased; as the d/a ratio decreased from -0.428 to -1.0

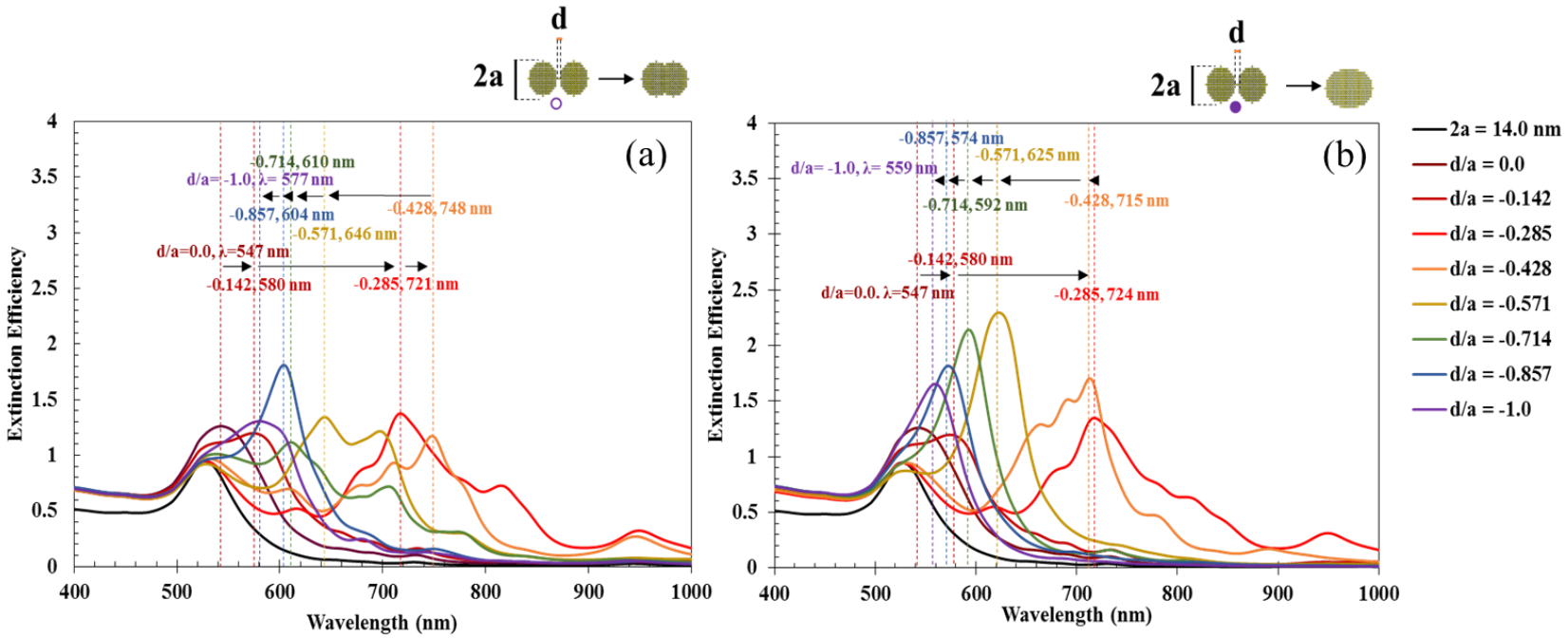

Figure 3.1 Extinction efficiency spectra for unpopulated (a) and repopulated (b) merged AuNS of 14 nm diameter. Dashed lines are placed for highest energy peaks in respect to d/a ratio.

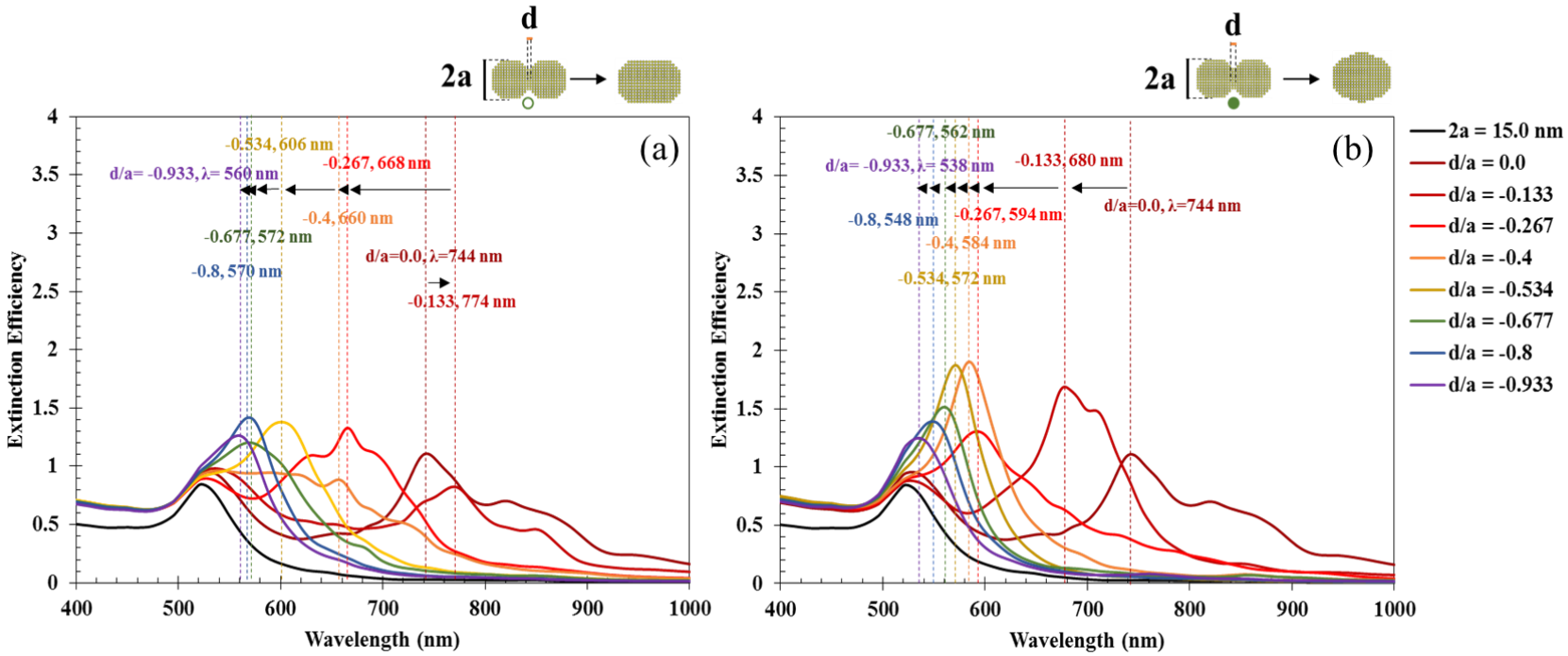

Figure 3.2 Extinction efficiency spectra for unpopulated (a) and repopulated (b) merged AuNS of 15 nm diameter. Dashed lines are placed for highest energy peaks in respect to d/a ratio.

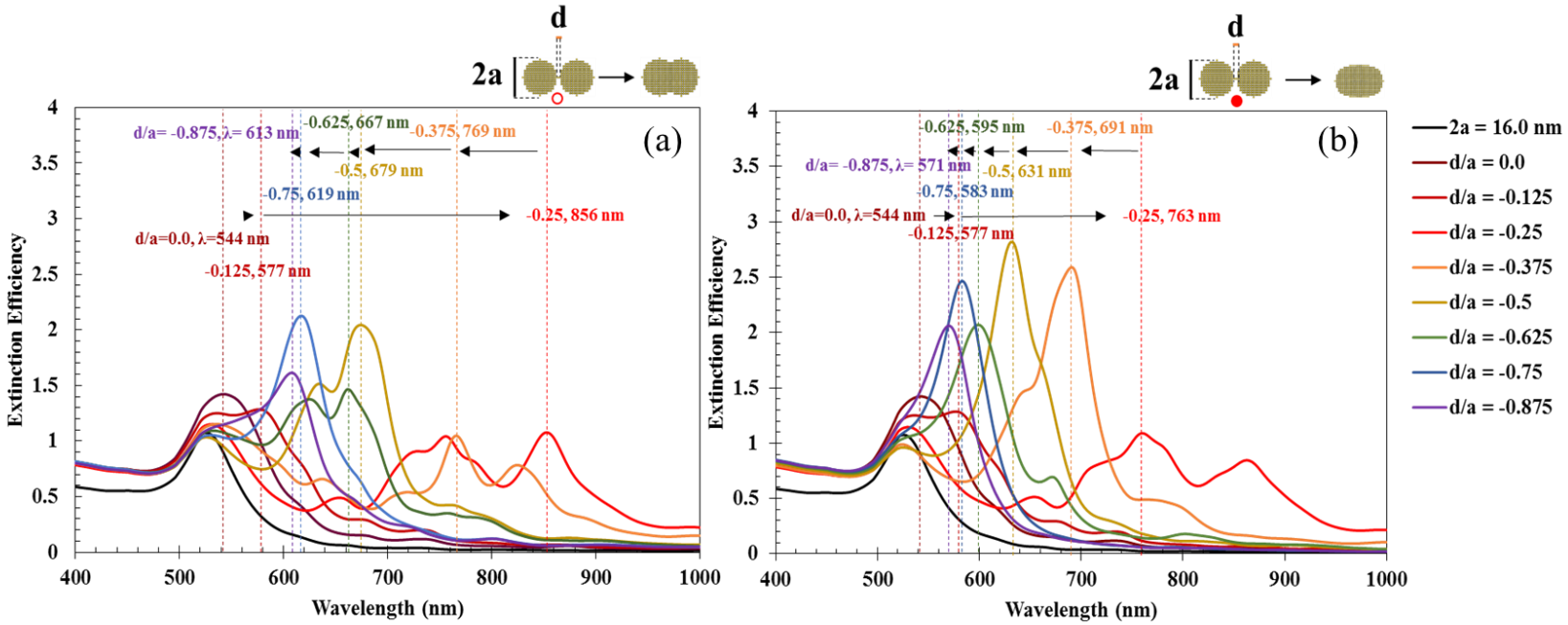

Figure 3.3 Extinction efficiency spectra for unpopulated (a) and repopulated (b) merged AuNS of 16 nm diameter. Dashed lines are placed for highest energy peaks in respect to d/a ratio.

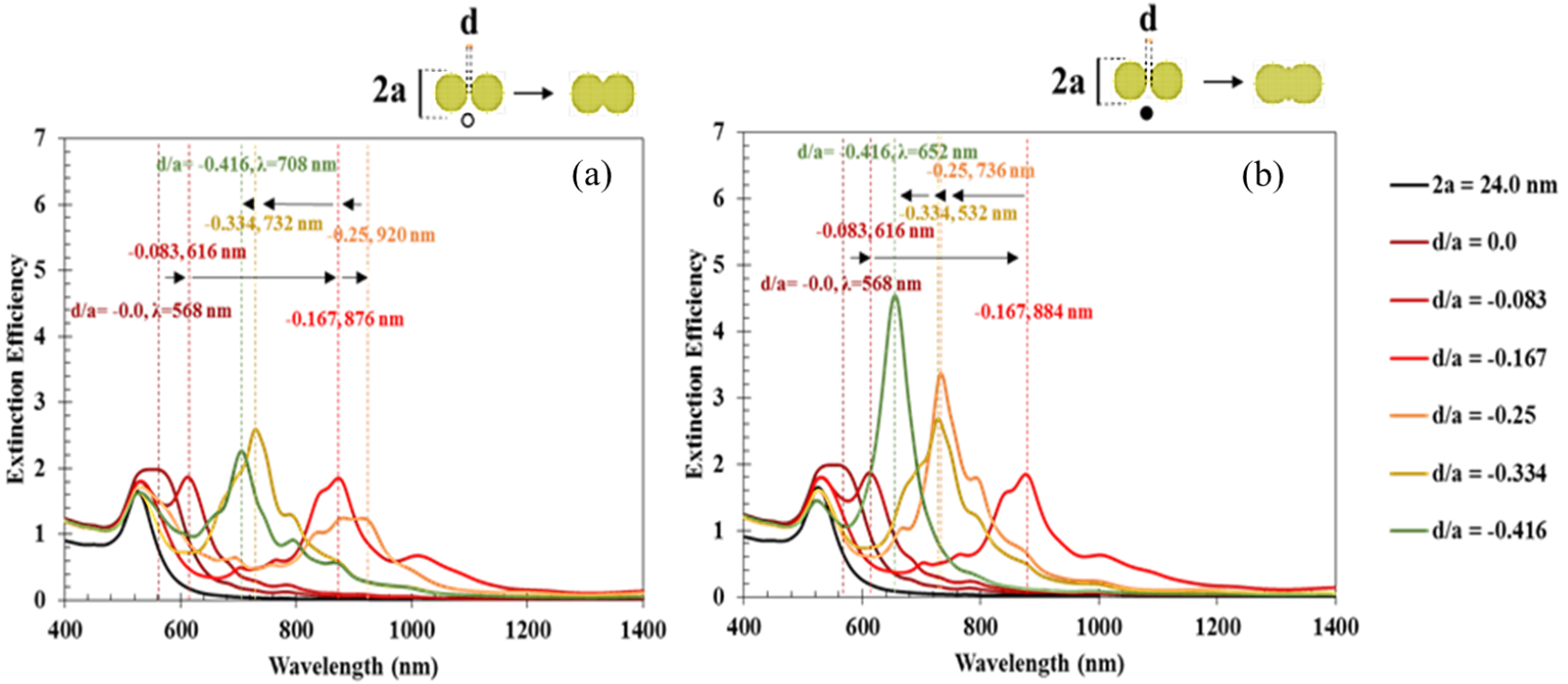

Figure 3.4 Extinction efficiency spectra for unpopulated (a) and repopulated (b) merged AuNS of 24 nm diameter. Dashed lines are placed for highest energy peaks in respect to d/a ratio.

(pair 8), the maximum L peak blue-shifted and the total number of optical features in the NIR decreased. This is also observed in Figure 3.4(b) with the d/a ratio decreasing from 0.0 to -0.285 (pair 3) resulting in a red-shift as well as an increase in optical features in the NIR and the d/a ratio decreasing from -0.285 to -1.0 (pair 8) resulting in a blue-shift as well as a decrease in the number of optical features in the NIR. As the two AuNSs transitioned from pair 1 to pair 8 (two AuNSs to one AuNR), the optical features adjacent to the maximum L peak combined and resulted in spectra consistent with literature for simulations of AuNRs [25,94,99]. These trends were also observed for dimers with radii of 7.5 (Figure 3.2), 8 (Figure 3.3), and 24 nm (Figure 3.4).

Dimers with higher cleft depth geometry resulted in an increase in the number of shoulders observed on the L peak and an increase in the number of optical features in the NIR, while dimers with lower cleft depth resulted in no observable optical features in the NIR and a reduction in the number of shoulders on the L peak. Figure 3.3(a) shows extinction efficiencies for six dimers (repopulated and unpopulated for 7, 7.5, and 8 nm AuNS radii) at the initial instance where more than two dipole points of each AuNS were in contact. At this instance, the cleft depth between the two AuNSs was at its highest value and resulted in the formation of multiple shoulders on the maximum L peak in the NIR. For simulations of AuNSs with whole number radii (7 and 8 nm), the shape generated resulted in a smooth, spherical structure that allowed for only two dipole points to be moved/removed at the initial emergence of the AuNSs.

However, for simulations of AuNSs with fractional radii (7.5 nm), the shape generated was not spherical and resulted in 22 dipole points being moved/removed at the initial emergence of the AuNSs. This resulted in an observable difference in the extinction efficiency spectra shown in Figure 3.5(a) for the AuNS with a radius of 7.5 nm (green solid and dashed lines)

compared to extinction efficiency spectra for AuNSs with radii of 7 (purple solid and dashed

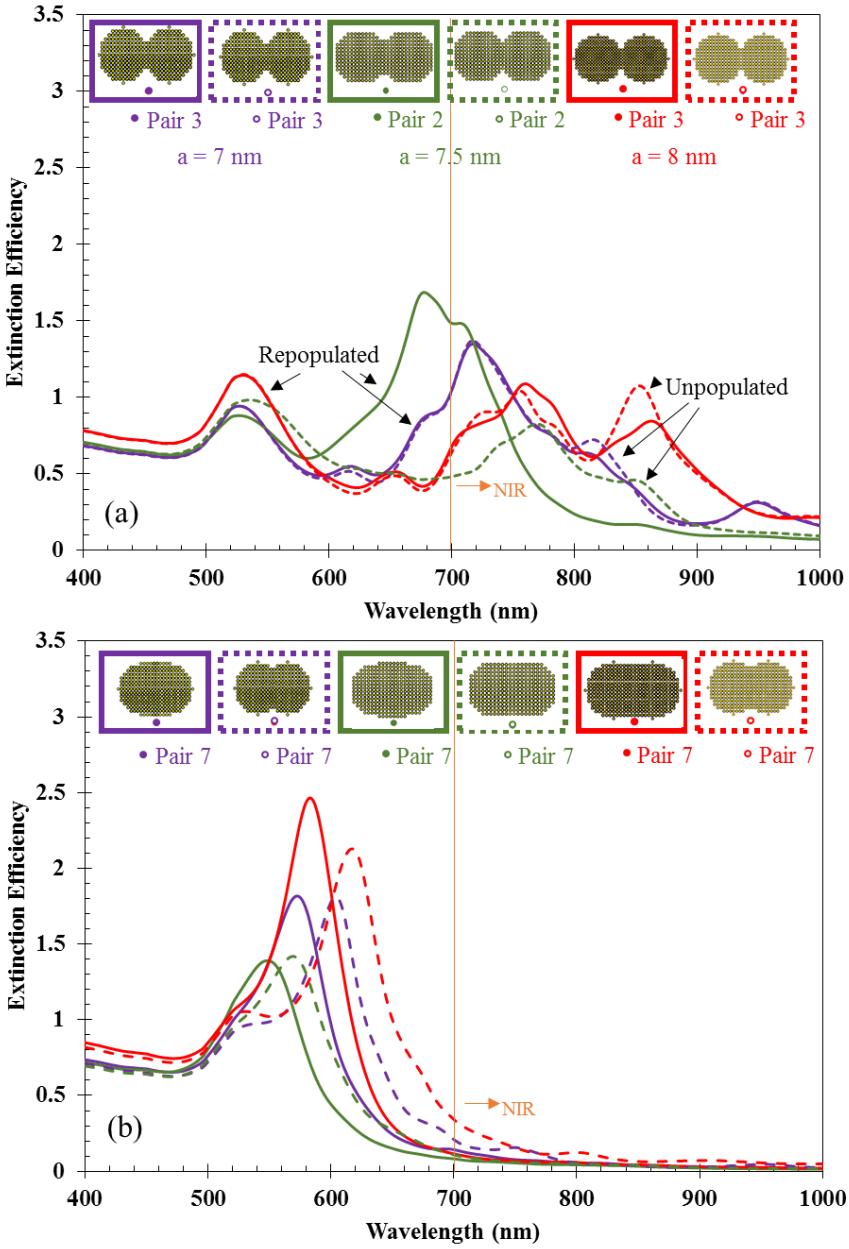

Figure 3.5 Symmetric cleft cavities for six dimers with sharp cleft depths (a) and shallow cleft depths (b). Symmetric cleft cavities for 14 (violet), 15 (green), and 16 (red) nm AuNSs dimers with deep antiwedge points have a higher number of multimodal wavelength peaks in the NIR when compared to shallow antiwedge points.

lines) and 8 nm (red solid and dashed lines). Figure 3.5(b) shows the extinction efficiencies for

six dimers at the instance the structures were most like an AuNR, which resulted in the maximum L peak blue-shifting by more than 150 nm and beginning to combine with the T peak.For AuNRs, the aspect ratio controls the optical properties where aspect ratios below 2 were reported to demonstrate the merging of the L and T peaks [25,40]. The dimers shown in Figure 3.5(b) had aspect ratios of ~1.5, which resulted in the observation of the merging of the two peaks. As these AuNSs merged toward the AuNR structure, the maximum L peak no longer exhibited multiple shoulders in the NIR (>700 nm wavelength) and was blue-shifted closer to peak locations of ~600 nm (as shown in Figure 3.5(b)).

3.2 Comparison of experimental and computational dimers

The ratio of the cleft depth (c) and the particle radius (a) for Au dimers with similar geometric dimensions produced less than 0.6 % difference error between simulated and experimental L and T peak locations. Figure 3.6(a) shows a TEM image consisting of a colloidal suspension of merged AuNS dimers (AuNS radii = ~7.4 ± 0.5 nm) fabricated via centrifugal force [24]. Simulations of dimers with AuNS radii of 7, 7.5, and 8 nm were performed based on the extracted dimensions of the dimers in the TEM image to determine and compare the extinction efficiencies to measured absorption spectra of the fabricated dimers. Similar studies have been reported by Chu et al. [70] and Su et al. [100] where SEM or STEM images were used to determine the size of the nanostructures for FDTD simulations and compared to measured optical properties. The extracted dimensions of the dimers shown in Figure 3.6(a) were used to determine a measured c/a ratio (listed outside the red boxes), which was used to select the dimers from simulations (shown as insets) that had the closest c/a ratio (listed inside the dashed boxes) to the measured values. While measured AuNS radii were ~7.5 nm, the simulations that resulted in the closest c/a ratios to the measured values consisted of unpopulated dimers with AuNSs with

and 8 nm radii. Optical properties of three of the simulated dimers (c/a = 0.571, 0.375 (used twice), 0.286) that closely matched measured values (c/a = 0.517, 0.368, 0.324, and 0.288) were

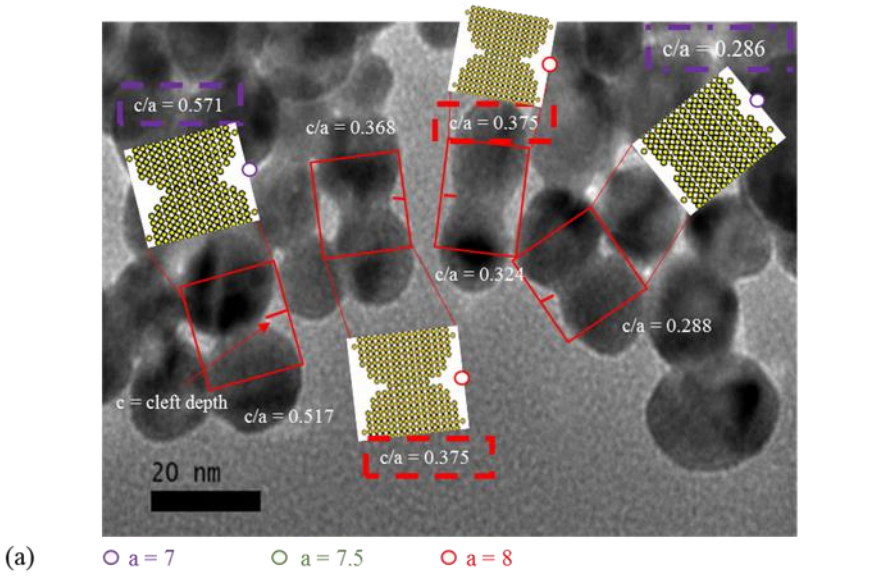

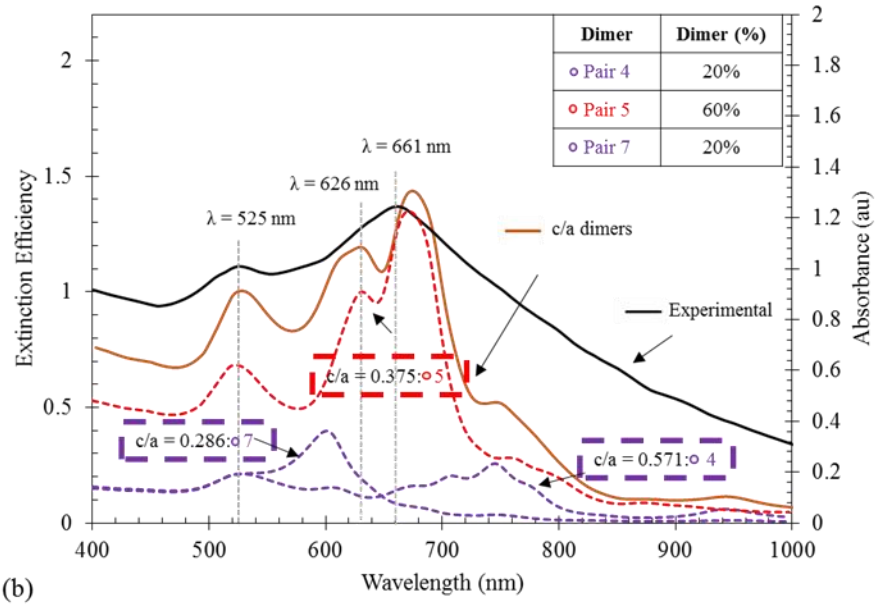

Figure 3.6 TEM of 15 nm AuNSs dimers spectra compared with computational dimers. a) TEM of 15 nm AuNSs merged via centripetal force with insets of simulated dimers with similar cleft depth/particle radius (c/a) ratio. b) Optical and simulated spectra that demonstrates < 0.6% error difference in the T and L peak.

combined to estimate and compare the T and maximum L peak locations to measured absorption

spectra as shown in Figure 3.6(b).

Initial estimates assumed that the measured absorption spectra were a combination of equal distributions of these three dimers, which resulted in 1.3% and 9.3% difference for the T (532 nm vs. 525 nm) and L (602 nm vs. 661 nm) peaks, respectively. Since one of the dimers was used twice, the percentages were adjusted to 25, 25, and 50% for the three dimers, which resulted in an improvement to 1.3% and 1.4% for the T (532 nm vs. 525 nm) and L (670 nm vs. 661 nm) peaks, respectively. Additional adjustments to the distribution percentages of the dimers resulted in less than 0.6% difference in both the T (526 nm vs. 525 nm) and L (661 nm vs. 665 nm) peak locations when the distribution percentages were 20, 20, and 60%.

3.3 Interface sensitivity from dimers

Redistributed charge around the dimer cleft region caused a change in the bright modes at the near infrared region. Relocating a minuscule number of dipole points at the cleft region for deep cleft depth dimers enhanced sensitivity to red or blue shift L peak and shoulders in NIR region. With the 4218 dipole point dimer, two dipole points were adjusted at symmetric (180°) and asymmetric (90°) displacement, causing a red and blue shift in the dampened 850 nm wavelength peak. In Figure 3.7, maximum wavelength peaks emerged at 841 nm and 863 nm when two dipole points were displaced in symmetrical (90°) and asymmetrical (180°) locations, respectively, at the interparticle junction area. When the two dipole points (orange dots) were introduced into the characterized dimer (d/a = -0.25) 3, the spectra tended to dampen the extinction efficiency by 0.24 AU. This descending spectra happened in the 850 nm range of the spectra and corresponded to the proximity of the displacement of the two dipole points in the interparticle junction area.

Additionally, the symmetrical (180°) dimer redshifted the wavelength peak by 11 nm,

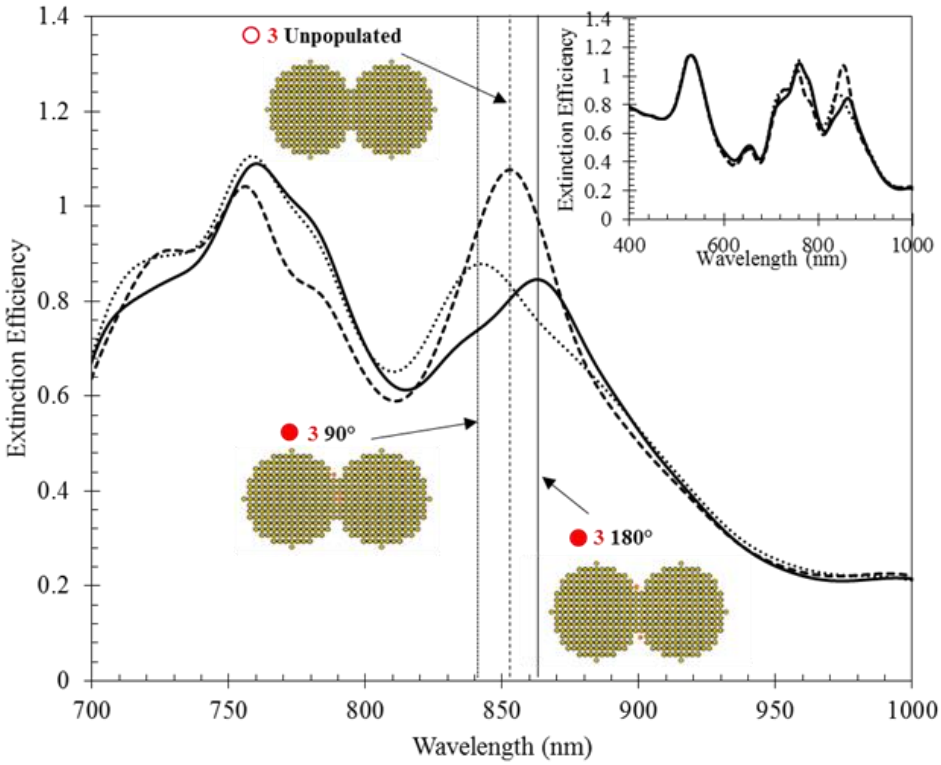

Figure 3.7 Dimer pair 3 with two adjusted dipole points in cleft region. A red and blue shift in the NIR region happens when dimer (d/a = -0.25) 3 has two adjusted dipole points in symmetrical (180°) and asymmetrical (90°) displacements. These dipole placements (light orange dots) were located at the cleft region.

while the asymmetrical (90°) dimer blue shifted by 11 nm as well. This damping and shifting of spectra with only two dipole points demonstrated some sensitivity of the interparticle junction area. This sensitivity behavior is comparable to nanoparticles with small interparticle gaps, where the extinction spectra significantly begin to red shift as the gap closes [30,102-108]. Atay et al. considered this interparticle junction area and an array of dimers as prime optical manipulations that provide an effective application to nonlinear optics [108]. In contrast, the inset demonstrates the extinction efficiency spectra range of 400-1000 nm for all three dimers. The extinction efficiency spectra below 700 nm, and above 900 nm had little to no significant damping or wavelength shifts.

3.4 Summary

In conclusion, nontoxic merged gold nanospheres dimers have the potential to be the leading cancer therapy through noninvasive ablation on diseased tumor cells. These dimers are explored via DDA with unpopulated and repopulated dipole points that show a strong variation of multimodal peaks in the NIR. These attributes are examined by merged AuNSs with spherical (diameter 14, 16 and 24 nm) and octagonal (diameter 15 nm) shapes, where a sharp transition from a single plasmon feature, the visible region, to a multimode feature, infrared region, arise when a cleft begins to form. Subsequently, the cleft depths of both schematic dimers and a transmission electron microscope (TEM) image of experimental dimers were correspondingly used to distinguish computational dimers that validated a less than 2% error difference for both combined computational spectra and experimental spectra. These correlations between DDA simulations with UV-vis spectroscopy validated the multimodal corresponding variations in NIR with the geometric configurations of the merged AuNSs

3.5 Computational preparation

3.5.1 Shape generation of Au dimers

The building of the Au dimers was performed using a custom-made shape generator tool (available on nanoHub.org) that provides target and parameter files for the structure used for the simulations. This tool provides a MATLAB code that offers five different predetermined shapes that could be generated for the simulations. For this work, the spherical shape was selected from the tool output window where the outer radius (7 nm), dipole spacing (1 nm), wavelength range (400-1000 nm), refractive index (RI) of material surrounding the shape (water, 1.33), and the dielectric function of the shape material (Au) were defined. This provided three files: (1) a plot of the shape generated (as shown in Figure 3.8-3.11); (2) a target file to alter the shape; and (3) a

parameter file (ddscat.par) to alter the parameters above as well as the polarizability. Average polarizability was selected within the parameter file, and the target file was used to duplicate the sphere to generate two spheres nearby. These spheres were merged to form dimers by either removing dipole points 1 nm at a time (unpopulated) or by moving the dipole points at the interparticle junction area (cleft) between the merging spheres to adjacent dipole points (repopulated). The additional dimers were generated at radii of 7.5, 8, and 12 nm, Figure 3.9, 3.10, 3.11, respectively, using this procedure. However, Figure 3.7 had the schematic for 15:15 dimers where the octagonal shape of the AuNSs reshaped the dimer figure into an AuNR and ovoid shape at a faster rate when compared to 14, 16, and 24 nm dimers. The refractive index was set as water, 1.33, to match the colloidal 15 nm diameter dimers [24].

3.5.2 DDA simulations using DDSCAT v7.3.

A 12-core supercomputer node with 64 GB memory was used to simulate the modified target and ddscat.par files generated as shown in Section 3.5.1. Extinction coefficients and RI values for Au were extracted from work performed by Johnson and Christy to generate a dielectric file [109]. DDSCAT (v7.3) was used to distinguish bright modes for all of the dimer pairs. The refractive index was performed with water (1.33). A command file (DDSCAT.pbs) was used to initiate and control the run-time of the simulations in the supercomputer. The dielectric file, command file, the modified target and parameter files, and the shape file were inserted into the supercomputer to begin the simulations for each of the dimers. Upon completion, the supercomputer outputs a file containing the extinction, absorption, and scattering efficiencies of the dimers versus wavelength. The data from these output files were transferred into Microsoft Excel, and the extinction efficiencies for each of the dimers were plotted versus wavelength and compared for unpopulated and repopulated merging procedures. Multiple

theoretical research has reported dimers surrounding medium to be similar to that of water (1.33), for these nanostructures tend to be in highly water solutions [110-114].

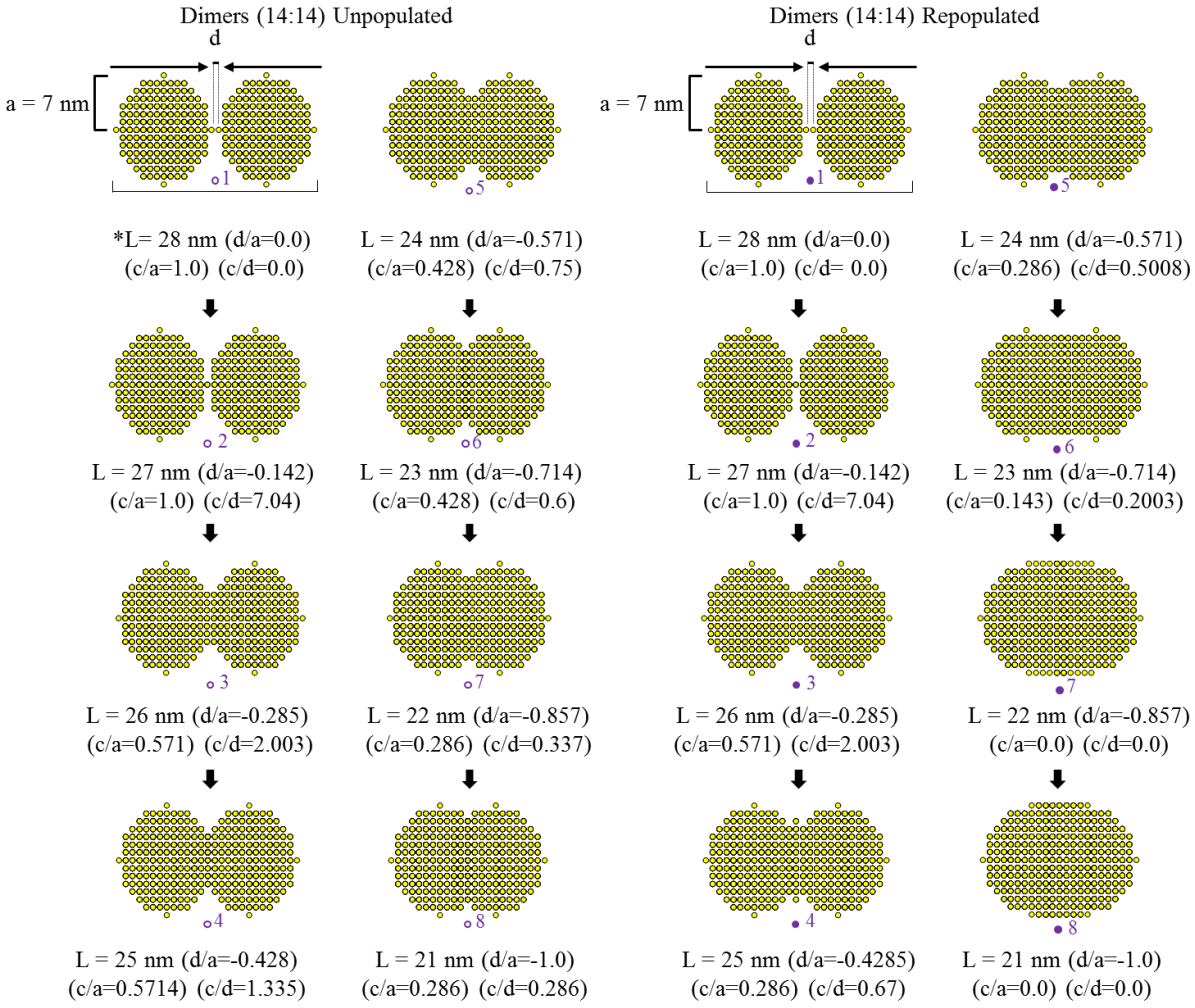

Figure 3.8 Schematics of Au dimers merging (unpopulated and repopulated) for 14 nm AuNS. Dimers unpopulated and repopulated show the radius (a) and the overlapped distance (d) in a nomenclature format (L = 4a + d) where L is the elongated length of the two nanoparticles combined. The colored dot at the bottom of the schematic dimers represents its correspondent AuNS radius: violet for 14 nm AuNS.

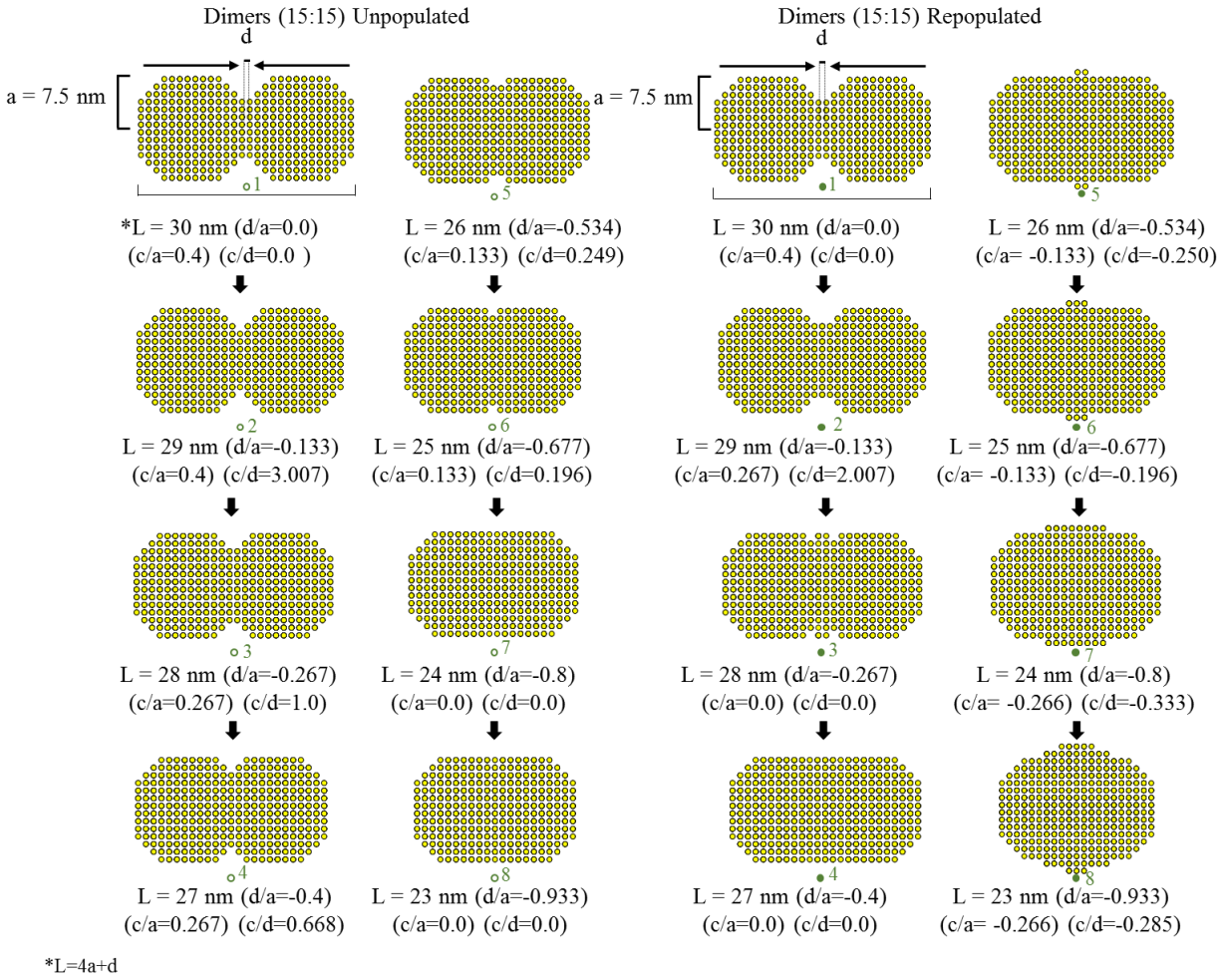

Figure 3.9 Schematics of Au dimers merging (unpopulated and repopulated) for 15 nm AuNS. Dimers unpopulated and repopulated show the radius (a) and the overlapped distance (d) in a nomenclature format (L = 4a + d) where L is the elongated length of the two nanoparticles combined. The colored dot at the bottom of the schematic dimers represents its correspondent AuNS radius: green for 15 nm AuNS.

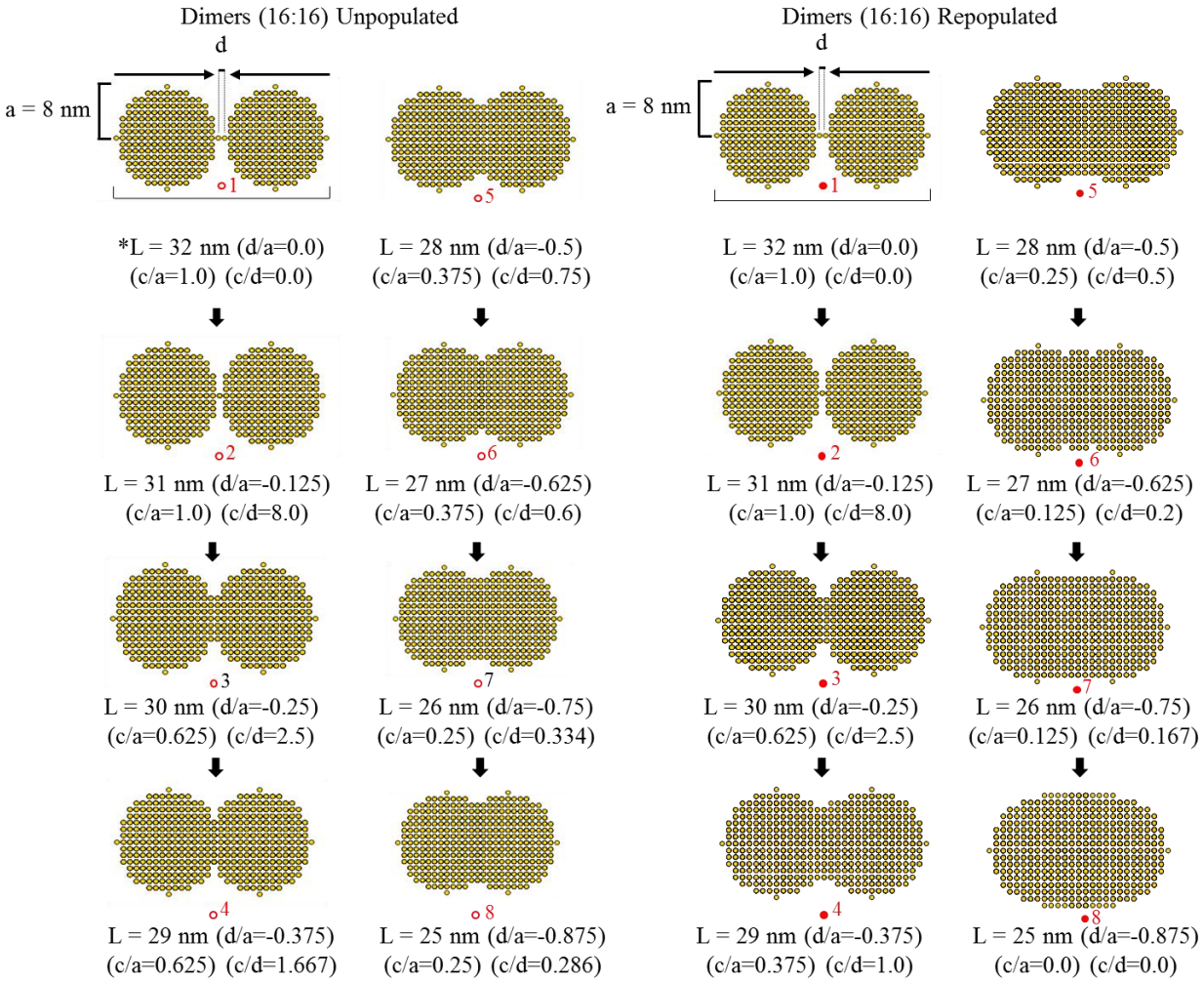

*L=4a+d

Figure 3.10 Schematics of Au dimers merging (unpopulated and repopulated) for 16 nm AuNS. Dimers unpopulated and repopulated show the radius (a) and the overlapped distance (d) in a nomenclature format (L = 4a + d) where L is the elongated length of the two nanoparticles combined. The colored dot at the bottom of the schematic dimers represents its correspondent AuNS radius: red for 16 nm AuNS.

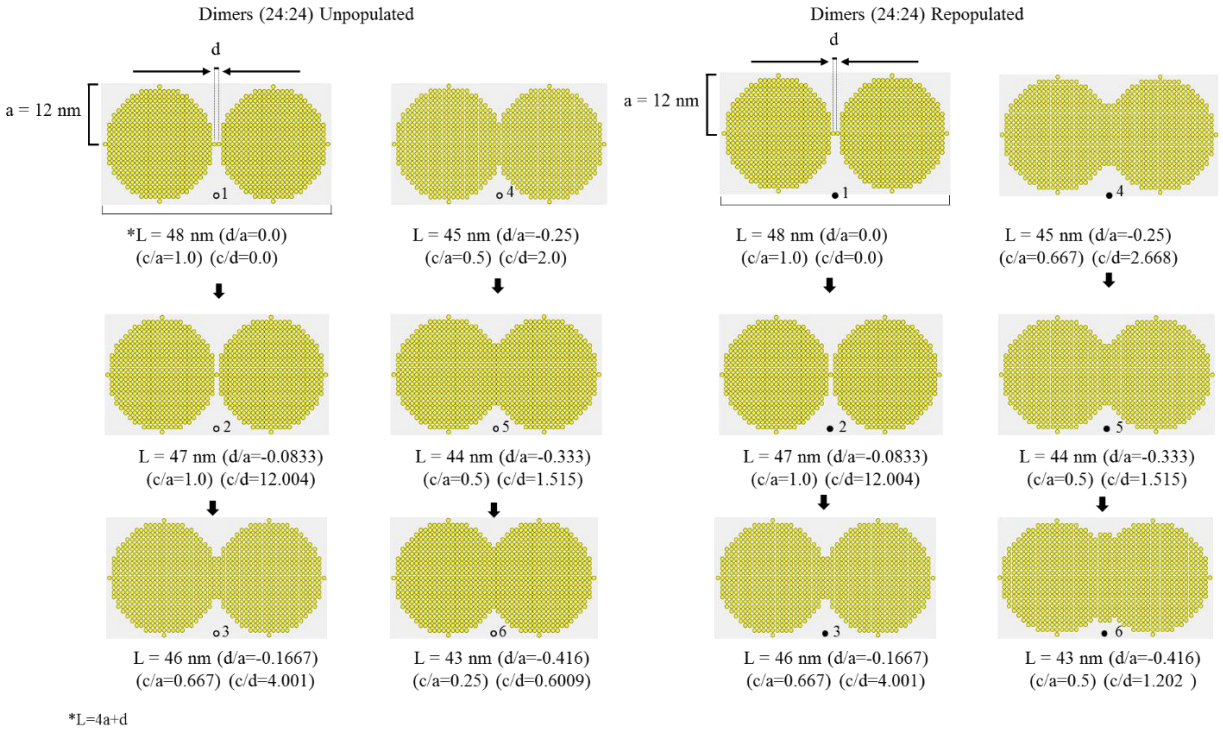

Figure 3.11 Schematics of Au dimers merging (unpopulated and repopulated) for 24 nm AuNS. Dimers unpopulated and repopulated show the radius (a) and the overlapped distance (d) in a nomenclature format (L = 4a + d) where L is the elongated length of the two nanoparticles combined. The colored dot at the bottom of the schematic dimers represents its correspondent AuNS radius: black for 24 nm AuNS.

4 Concluding Remarks

This thesis describes the research on the fabrication, design considerations, and characterization of nanostructured nanoantennae, specifically the noble metal-semiconductor and noble metal-noble metal combinations. The noble metal-semiconductor and noble metal-noble metal nanoantennae have experimentally and computationally shown enhanced optical features via a combination of excitons and plasmons. The cost-effective techniques performed to produce the 2D TMD-metal nanocrystals and the theoretical computation have effectively demonstrated the ability for these nanoantennae combinations to enhance the optical features for optoelectronics and biomedical engineering. This chapter will discuss the importance of the research performed, results obtained, and ideas for future work based on the enhanced optical properties from these heterostructures.

4.1 Importance of work

Fossil fuels have dominated global energy for many years and have produced major concerns over the increased carbon dioxide emission in the earth's atmosphere. Key goals to reduce the carbon footprint are making alternative energies readily available for efficient macroscale production. Wind, solar, and geothermal energy technologies have recently attained significant improvements in reducing the carbon footprint with plasmonic nanostructures [2,3]. However, the enhancements (e.g. excitons, surface plasmon resonances) from these nanostructures have lagged due to the high cost of producing these materials (e.g., electron beam lithography, chemical vapor deposition). Part of this work has focused on performing an alternative method to determine the optimal geometric nanostructure that produces optical enhancements such as LSPR in the NIR region. With inexpensive nanoantennae (e.g., noble metal-noble metal (dimers) and noble meta-semiconductor heterostructures (e.g. Pt-WS_2)) an

efficient level of optical emissions arise. These nanoantennae have been studied theoretically and experimentally. Optical emissions have a higher energy and cover a broader ultraviolet-visible-near infrared range of the electromagnetic spectra due to the combination of these nanostructures.

Cancer results in approximately eight million deaths yearly and a demanding solution to manage it has been a primary focus in biomedical engineering. Nanotechnology has demonstrated promise for cancer therapy through noninvasive ablation on diseased tumor cells via light-activated therapies. Au nanostructures show potential with their electromagnetic and optical properties to ablate malignant cells through plasmonic photothermal therapy (PPTT). They also show promise with the immunotherapeutic application, where delivery of immunomodulation materials (i.e., antigens, checkpoint inhibitors, and cytokines) assist with mitigating the cancerous cells. An adequate amount of progress has been performed to mitigate tumors with toxic cetyltrimethylammonium bromide (CTAB) and silver nitrate growth conditions. However, these harmful synthesis methods can cause a significant problem for humans. A solution is to use citrate-coated gold nanospheres (AuNSs) merged via centripetal force. These overlapping AuNSs have optically demonstrated visible to near infrared region (NIR) optical features that can rival the current nanostructures. In this study, the new distinct features that arise in the nanodimers have been investigated theoretically via DDA. These distinguishing features in merged AuNSs have demonstrated key longitudinal wavelength peaks in the NIR region, which can be attained by specific geometric configurations of the nanodimers. These nanodimers have the potential to broaden the medical community use of alternative nontoxic nanostructures for tumor mitigations.

4.2 Research summary

The creation of 2D transition metal dichalcogenides nanoflakes via the probe and freeze-and-thaw liquid phase exfoliation was successfully demonstrated to be a cost effective route. 2D WS_2 decorated with PtNPs via a reduction technique was characterized with TEM, SEM, EDS mapping, and optical absorbance. The characterization effectively demonstrated the production of the noble metal - semiconductor heterostructure, which indicated that the average PtNP size decorated at the edge and basal parts of the 2D nanosheet observed in the presence of halogen irradiation could be attributable to the photoelectric effect. Additionally, optical extinction and absorbance spectra determined the unique enhanced optical features (e.g., excitons and SPR) are predominately present at the UV-Vis EM range.

The dimers were explored via DDA with unpopulated and repopulated dipole points that show a strong variation of multimodal peaks in the Vis-NIR region. The cleft depths, antiwedge area, from both schematic dimers and a transmission electron microscope (TEM) image of experimental dimers were correspondingly used to distinguish computational dimers which validated a less than 2% error difference for both combined computational and experimental spectra.

4.3 Future work

Extending across the broad range of the electromagnetic field, the studied nanostructures covered ultraviolet (via PtNPs), visible (via Pt-Au-WS_2), and near-infrared (Au-Au) regions. Having this potential allows theses nanostructures to be further studied as a catalyst. Studies have indicated the Pt-WS_2 could readily be combined with Nafion (Nafion D-521, Beantown Chemical, Hudson, NH) and Ketjen (Carbon black, Akzo Nobel Functional Chemicals, Chicago, IL) to produce a co catalyst ink for producing hydrogen fuel cells via hydrogen evolution

reaction. The nanoantennae could also be characterized under a scanning transmission electron microscope to perform electron energy loss spectroscopy (EELS). EELS has the potential to expose the material with an electron beam and make the paths of the electrons randomly and slightly deflected due to the geometric surface of the nanoantennae. The pathways of the electrons are then plotted with an electron energy loss spectrum. EELS spectra can be obtained for these heterostructures theoretically with electron discrete dipole approximation (eDDA). Masiello and Henrard implemented and adapted the DDA algorithm to electron-excitation, called eDDA and DDEELS [115,116]. The nanostructure gets excitation by an electron at a certain location (impact point) on the nanoantenna. This impact point, composed of electrons, induces resonances not observable under light excitation, also known as dark modes. Each impact point produces a spatially-unique bright or dark plasmon resonance mode in the electromagnetic loss density of state (ELDOS). The plasmonic nanoantenna, in this case, dimers or Pt-WS_2, influences the ELDOS since unique multi plasmonic features arise in the DDA spectra. Distinguishing, which unique geometric location on the nanoantenna contributes to the bright modes will establish certainty on optimizing the heterostructures geometry to attain better optical features.

References

1. S. Chu and A. Majumdar, "Opportunities and challenges for a sustainable energy future," Nature **488**(7411), 294-303 (2012).

2. J. P. Hansen, P. A. Narbel, and D. L. Aksnes, "Limits to growth in the renewable energy sector," Renew. Sustain. Energy Rev. **70**(16), 769-774 (2017).

3. D. P. van Vuuren, E. Stehfest, D. E. H. J. Gernaat, J. C. Doelman, M. van den Berg, M. Harmsen, H. S. de Boer, L. F. Bouwman, V. Daioglou, O. Y. Edelenbosch, B. Girod, T. Kram, L. Lassaletta, P. L. Lucas, H. van Meijl, C. Müller, B. J. van Ruijven, S. van der Sluis, and A. Tabeau, "Energy, land-use and greenhouse gas emissions trajectories under a green growth paradigm," Glob. Environ. Chang. **42**, 237-250 (2017).

4. I. Thacker and G. Sinatra, "Visualizing the Greenhouse Effect: Restructuring Mental Models of Climate Change Through a Guided Online Simulation," Educ. Sci. **9**(1), 14 (2019).

5. N. S. Lewis, "Toward Cost-Effective Solar Energy Use," Science **315** (5813) (2007), 798-801 (2013).

6. M. G. Walter, E. L. Warren, J. R. McKone, S. W. Boettcher, Q. Mi, E. A. Santori, and N. S. Lewis, "Solar water splitting cells," Chem. Rev. **110**(11), 6446-6473 (2010).

7. N. L. Panwar, S. C. Kaushik, and S. Kothari, "Role of renewable energy sources in environmental protection: A review," Renew. Sustain. Energy Rev. **15**(3), 1513-1524 (2011).

8. B. D. Solomon and K. Krishna, "The coming sustainable energy transition: History, strategies, and outlook," Energy Policy **39**(11), 7422-7431 (2011).

9. K. H. Solangi, M. R. Islam, R. Saidur, N. A. Rahim, and H. Fayaz, "A review on global solar energy policy," Renew. Sustain. Energy Rev. **15**(4), 2149-2163 (2011).

10. E. Cao, W. Lin, M. Sun, W. Liang, and Y. Song, "Exciton-plasmon coupling interactions: From principle to applications," Nanophotonics **7**(1), 145-167 (2018).

11. D. Voiry, H. Yamaguchi, J. Li, R. Silva, D. C. B. Alves, T. Fujita, M. Chen, T. Asefa, V. B. Shenoy, G. Eda, and M. Chhowalla, "Enhanced catalytic activity in strained chemically exfoliated WS_2 nanosheets for hydrogen evolution," Nat. Mater. **12**(9), 850-855 (2013).

12. H. Lv, Z. Xi, Z. Chen, S. Guo, Y. Yu, W. Zhu, Q. Li, X. Zhang, M. Pan, G. Lu, S. Mu, and S. Sun, "A New Core/Shell NiAu/Au Nanoparticle Catalyst with Pt-like Activity for Hydrogen Evolution Reaction," J. Am. Chem. Soc. **137**(18), 5859-5862 (2015).

13. X. Guo, Y. Hou, R. Ren, and J. Chen, "Temperature-dependent Crystallization of MoS2 Nanoflakes on Graphene Nanosheets for Electrocatalysis," Nanoscale Res. Lett. **12**, 479-485 (2017).

14. M. G. Walter, E. L. Warren, J. R. McKone, S. W. Boettcher, Q. Mi, E. A. Santori, and N. S. Lewis, "Solar water splitting cells," Chem. Rev. **110**(11), 6446-6473 (2010).

15. H. A. Atwater and A. Boltasseva, "Low-Loss Plasmonic Metamaterials," Science (80-.) **331**(1), 290-291 (2011).

16. E. Ozbey, "Plasmonics : Merging Photonics and Electronics at the nanoscale dimensions," Science (80-.) **311**(5758), 189-194 (2006).

17. T. Vo-Dinh, "Shining Gold Nanostars: From Cancer Diagnostics to Photothermal Treatment and Immunotherapy," J. Immunol. Sci. **2**(1), 1-8 (2018).

18. L. Tong, Y. Zhao, T. B. Huff, M. N. Hansen, A. Wei, and J. X. Cheng, "Gold nanorods mediate tumor cell death by compromising membrane integrity," Adv. Mater. **19**(20), 3136-3141 (2007).

19. B. Navyatha and S. Nara, "Gold nanostructures as cancer theranostic probe: promises and hurdles," Nanomedicine **14**(6) 170-181(2019).

20. X. Huang, P. K. Jain, I. H. El-Sayed, and M. A. El-Sayed, "Plasmonic photothermal therapy (PPTT) using gold nanoparticles," Lasers Med. Sci. **23**(3), 217-228 (2008).

21. D. P. O'Neal, L. R. Hirsch, N. J. Halas, J. D. Payne, and J. L. West, "Photo-thermal tumor ablation in mice using near infrared-absorbing nanoparticles," Cancer Lett. **209**(2), 171-176 (2004).

22. E. R. Evans, P. Bugga, V. Asthana, and R. Drezek, "Metallic nanoparticles for cancer immunotherapy," Mater. Today **21**(6), 673-685 (2018).

23. J. Wan, J. H. Wang, T. Liu, Z. Xie, X. F. Yu, and W. Li, "Surface chemistry but not aspect ratio mediates the biological toxicity of gold nanorods in vitro and in vivo," Sci. Rep. **5**(May), 1-16 (2015).

24. J. N. Batta-Mpouma, "Inertial Force-Driven Synthesis of Near-Infrared Plasmonic Nanosphere Composites: Physicochemical Characterizations," University of Arkansas Thesis (2015).

25. X. Xu and M. B. Cortie, "Shape change and color gamut in gold nanorods, dumbbells, and dog bones," Adv. Funct. Mater. **16**(16), 2170-2176 (2006).

26. Liu and P. Guyot-Sionnest, "Synthesis and Optical Characterization of Au/Ag Core/Shell Nanorods," J. Phys. Chem. B **108**(19), 5882-5888 (2004).

27. C. C. Huang, Z. Yang, and H. T. Chang, "Synthesis of dumbbell-shaped Au-Ag core-shell nanorods by seed-mediated growth under alkaline conditions," Langmuir **20**(15), 6089-6092 (2004).

28. L. Gou and C. J. Murphy, "Fine-tuning the shape of gold nanorods," Chem. Mater. **17**(14), 3668-3672 (2005).

29. N. F. Scherer, S. K. Gray, R. A. Nome, and M. J. Guffey, "Plasmonic Interactions and Optical Forces between Au Bipyramidal Nanoparticle Dimers," J. Phys. Chem. A **113**, 4408-4415 (2009).

30. Z. Shen and L. Su, "Plasmonic trapping and tuning of a gold nanoparticle dimer," Opt. Express **24**(5), 4801 (2016).

31. D. DeJarnette, D. K. Roper, and B. Harbin, "Geometric effects on far-field coupling between multipoles of nanoparticles in square arrays," J. Opt. Soc. Am. B **29**(1), 88 (2012).

32. A. D. andThomas W. E. William L. Barnes, "Subwavelength Optics," F. Guid. to Digit. Micro-Optics **424**(August), 824-830 (2015).

33. J. Hee Song, F. Kim, D. Kim, and P. Yang, "Crystal overgrowth on gold nanorods: Tuning the shape, facet, aspect ratio, and composition of the nanorods," Chem. - A Eur. J. **11**(3), 910-916 (2005).

34. F. Huang and J. J. Baumberg, "Actively tuned plasmons on elastomerically driven Au nanoparticle dimers," Nano Lett. **10**(5), 1787-1792 (2010).

35. O. Neumann, A. D. Neumann, E. Silva, C. Ayala-Orozco, S. Tian, P. Nordlander, N. J. Halas, C. W. V. Gmbh, C. Kgaa, R. L. Martin, T. F. Willems, J. Kim, J. A. Swisher, and B. Smit, "Nanoparticle-mediated, light-induced phase separations," Nano Lett. **15**(12), 7880-7885 (2015).

36. A. L. González, J. A. Reyes-Esqueda, and C. Noguez, "Optical properties of elongated noble metal nanoparticles," J. Phys. Chem. C **112**(19), 7356-7362 (2008).

37. C. C. D. Wang, W. C. H. Choy, C. Duan, D. D. S. Fung, W. E. I. Sha, F. X. Xie, F. Huang, and Y. Cao, "Optical and electrical effects of gold nanoparticles in the active layer of polymer solar cells," J. Mater. Chem. **22**(3), 1206-1211 (2012).

38. D. K. Roper, J. Dunklin, and A. O. Brien, "Enhanced Catalysis by Optical Nanoantenna Reduced on Transition Metal Dichalcogenide," Nano-Micro Conference, 2017,1, 01003. doi:1011605/cp.nmc2017.01003.

39. J. R. Dunklin, P. Lafargue, T. M. Higgins, G. T. Forcherio, M. Benamara, N. McEvoy, D. K. Roper, J. N. Coleman, Y. Vaynzof, and C. Backes, "Production of monolayer-rich gold-decorated 2H-WS2 nanosheets by defect engineering," npj 2D Mater. Appl. **1**(1), 43 (2017).

40. S. Link, M. B. Mohamed, and M. A. El-Sayed, "Simulation of the Optical Absorption Spectra of Gold Nanorods as a Function of Their Aspect Ratio and the Effect of the Medium Dielectric Constant," J. Phys. Chem. B **103**(16), 3073-3077 (2002).

41. S. Sheikholeslami, Y. W. Jun, P. K. Jain, A. P. Alivisatos, N. F. Scherer, S. K. Gray, R. A. Nome, M. J. Guffey, F. Huang, J. J. Baumberg, J. Hee Song, F. Kim, D. Kim, P. Yang, X. Xu, and M. B. Cortie, "Coupling of optical resonances in a compositionally asymmetric plasmonic nanoparticle dimer," Nano Lett. **10**(3), 1787-1792 (2010).

42. K. F. Mak, C. Lee, J. Hone, J. Shan, and T. F. Heinz, "Atomically thin MoS_2: A new direct-gap semiconductor," Phys. Rev. Lett. **105**(13), 2-5 (2010).

43. R. F. Frindt and A. D. Yoffe, "Physical Properties of Layer Structures : Optical Properties and Photoconductivity of Thin Crystals of Molybdenum Disulphide," Royal Society **273**(1352) 69-83 (1963).

44. R. R. Frindt, "Optical Absorption of a Few Unit-Cell Layers of MoS_2," American Physical

Society Review **140**(October), 536-539 (1965).

45. R. F. Frindt, "Single crystals of MoS_2 several molecular layers thick," J. Appl. Phys. **37**(4), 1928-1929 (1966).

46. J. M. Raimond, M. Brune, Q. Computation, F. De Martini, and C. Monroe, "Electric Field Effect in Atomically Thin Carbon Films," Nature **306**(October), 666-670 (2004).

47. T. F. Jaramillo, K. P. Jørgensen, J. Bonde, J. H. Nielsen, S. Horch, and I. Chorkendorff, "Identification of active edge sites for electrochemical H_2 evolution from MoS_2 nanocatalysts," Science (80-.) **317**(5834), 100-102 (2007).

48. K. Manna, H. N. Huang, W. T. Li, Y. H. Ho, and W. H. Chiang, "Toward Understanding the Efficient Exfoliation of Layered Materials by Water-Assisted Cosolvent Liquid-Phase Exfoliation," Chem. Mater. **28**(21), 7586-7593 (2016).

49. B. Radisavljevic, M. B. Whitwick, and A. Kis, "Integrated Circuits and Logic Operations Based on Single-Layer MoS_2," ACS Nano. **5**(12), 9934-9938 (2011).

50. L. M. Malard, T. V. Alencar, A. P. M. Barboza, K. F. Mak, and A. M. De Paula, "Observation of intense second harmonic generation from MoS_2 atomic crystals," Phys. Rev. B - Condens. Matter Mater. Phys. **87**(20), 1-5 (2013).

51. J. N. Coleman, M. Lotya, A. O'Neill, S. D. Bergin, P. J. King, U. Khan, K. Young, A. Gaucher, S. De, R. J. Smith, I. V Shvets, S. K. Arora, G. Stanton, H.-Y. Kim, K. Lee, G. T. Kim, G. S. Duesberg, T. Hallam, J. J. Boland, J. J. Wang, J. F. Donegan, J. C. Grunlan, G. Moriarty, A. Shmeliov, R. J. Nicholls, J. M. Perkins, E. M. Grieveson, K. Theuwissen, D. W. McComb, P. D. Nellist, and V. Nicolosi, "Two-dimensional nanosheets produced by liquid exfoliation of layered materials.," Science **331**(6017), 568-571 (2011).

52. R. Suzuki, M. Sakano, Y. J. Zhang, R. Akashi, D. Morikawa, A. Harasawa, K. Yaji, and K. Kuroda, "Valley-dependent spin polarization in bulk MoS_2 with broken inversion symmetry," Nat. Nanotechnol. **9**(8), 611-617 (2014).

53. M. Acerce, D. Voiry, and M. Chhowalla, "Metallic 1T phase MoS 2 nanosheets as supercapacitor electrode materials," Nat. Nanotechnol. **10**(4), 313-318 (2015).

54. Y. Kang, S. Najmaei, Z. Liu, Y. Bao, Y. Wang, X. Zhu, N. J. Halas, P. Nordlander, P. M. Ajayan, J. Lou, and Z. Fang, "Plasmonic Hot Electron Induced Structural Phase Transition in a MoS_2 Monolayer," Adv. Mater. **26**(37), 6467-6471 (2014).

55. G. Eda, H. Yamaguchi, D. Voiry, T. Fujita, M. Chen, and M. Chhowalla, "Photoluminescence from chemically exfoliated MoS 2," Nano Lett. **11**(12) 5111-5116 (2011).

56. L. Niu, J. N. Coleman, H. Zhang, H. Shin, and M. Chhowalla, "Production of Two-Dimensional Nanomaterials via Liquid-Based Direct Exfoliation," Nano Micro Small (3), 272-293 (2016).

57. J. Shen, Y. He, J. Wu, C. Gao, K. Keyshar, X. Zhang, Y. Yang, M. Ye, R. Vajtai, J. Lou, and P. M. Ajayan, "Liquid Phase Exfoliation of Two-Dimensional Materials by Directly Probing and Matching Surface Tension Components," Nano Lett. **15**(8), 5449-5454

(2015).

58. O. V. Yazyev and A. Kis, "MoS_2 and semiconductors in the flatland," Mater. Today **18**(1), 20-30 (2015).

59. E. Simsek, B. Mukherjee, Z. Chen, and K. Gacem, "Visibility of dichalcogenide nanolayers," Nanotechnology **22**(12), 21-26 (2011).

60. H. Tsai, J. Heising, J. L. Schindler, C. R. Kannewurf, and M. G. Kanatzidis, "Exfoliated - Restacked Phase of WS_2 as pyridine , ammonia , etc . This intercalative inertness originates from the prismatic coordination environment of Mo and W centers (d2 configuration) which results in a fully occupied valence band composed of dz," Journal of American Chemical Society **4756**(96), 879-882 (1997).

61. C. Backes, B. M. Szydłowska, A. Harvey, S. Yuan, V. Vega-Mayoral, B. R. Davies, P. L. Zhao, D. Hanlon, E. J. G. Santos, M. I. Katsnelson, W. J. Blau, C. Gadermaier, and J. N. Coleman, "Production of highly monolayer enriched dispersions of liquid-exfoliated nanosheets by liquid cascade centrifugation," ACS Nano **10**(1), 1589-1601 (2016).

62. C. Backes, R. J. Smith, N. McEvoy, N. C. Berner, D. McCloskey, H. C. Nerl, A. O'Neill, P. J. King, T. Higgins, D. Hanlon, N. Scheuschner, J. Maultzsch, L. Houben, G. S. Duesberg, J. F. Donegan, V. Nicolosi, and J. N. Coleman, "Edge and confinement effects allow in situ measurement of size and thickness of liquid-exfoliated nanosheets," Nat. Commun. **5**, 1-10 (2014).

63. D. K. Roper, W. Ahn, and M. Hoepfner, "Microscale heat transfer transduced by surface plasmon resonant gold nanoparticles," J. Phys. Chem. C **111**(9), 3636-3641 (2007).

64. G. T. Forcherio and D. K. Roper, "Optical attenuation of plasmonic nanocomposites within photonic devices," Appl. Opt. **52**(25), 6417 (2013).

65. C. E. Dungey and C. F. Bohren, "Light scattering by nonspherical particles: a refinement to the coupled-dipole method," J. Opt. Soc. Am. A **8**(1), 81 (1991).

66. B. T. Draine and P. J. Flatau, "User Guide for the Discrete Dipole Approximation Code DDSCAT.6.0," Available from: <http://arxiv.org/ags.astro-ph/0309069> **1**(1994), 78 (2003). Accessed date: [March 18, 2017]

67. V. Myroshnychenko, J. Rodríguez-Fernández, I. Pastoriza-Santos, A. M. Funston, C. Novo, P. Mulvaney, L. M. Liz-Marzán, and F. J. García De Abajo, "Modelling the optical response of gold nanoparticles," Chem. Soc. Rev. **37**(9), 1792-1805 (2008).

68. O. S. Vartia, P. Ylä-Oijala, J. Markkanen, S. Puupponen, A. Seppälä, A. Sihvola, and T. Ala-Nissila, "On the applicability of discrete dipole approximation for plasmonic particles," J. Quant. Spectrosc. Radiat. Transf. **169**, 23-35 (2016).

69. S. Lal, I. Romero, D. W. Brandl, N. J. Halas, P. Nordlander, L. I. Hernandez, J. B. Lassiter, J. Aizpurua, and J. H. Hafner, "Close Encounters between Two Nanoshells," Nano Lett. **8**(4), 1212-1218 (2008).

70. M.-W. Chu, V. Myroshnychenko, F. Javier García de Abajo, and C. H. Chen, "Probing bright and dark surface plasmon modes in individual and coupled Au nanoparticles using

a fast electron beam," EMC 2008 14th Eur. Microsc. Congr. 1-5 Sept. 2008, Aachen, Ger. 361-362 (2009).

71. I. Romero, J. Aizpurua, G. W. Bryant, and F. J. G. De Abajo, "Plasmons in nearly touching metallic nanoparticles : singular response in the limit of touching dimers," Optics Express. **14**(21), 9988-9999 (2006).

72. V. S. Makadia, L. M. Manocha, S. Manocha, and H. L. Gajera, "The freeze-thaw technique for exfoliation of graphite: A novel approach for bulk production of scroll-free graphene oxide sheets," Adv. Mater. Lett. **8**(3), 262-264 (2017).

73. A. K. Mishra, K. V. Lakshmi, and L. Huang, "Eco-friendly synthesis of metal dichalcogenides nanosheets and their environmental remediation potential driven by visible light," Sci. Rep. **5**(October), 1-8 (2015).

74. L. Pan, Y. T. Liu, X. M. Xie, and X. Y. Ye, "Facile and Green Production of Impurity-Free Aqueous Solutions of WS2 Nanosheets by Direct Exfoliation in Water," Small **12**(48), 6703-6713 (2016).

75. M. V. Bracamonte, G. I. Lacconi, S. E. Urreta, and L. E. F. Foa Torres, "On the nature of defects in liquid-phase exfoliated graphene," J. Phys. Chem. C **118**(28), 15455-15459 (2014).

76. R. T. Timmer and J. M. Sands, "Lithium intoxication," J. Am. Soc. Nephrol. **10**(3), 666-674 (1999).

77. Y. Qian, C. Wang, and Z. G. Le, "Decorating graphene sheets with Pt nanoparticles using sodium citrate as reductant," Appl. Surf. Sci. **24**(257), 10758-10762 (2011).

78. Z. Lv, X. Yang, and E. Wang, "Highly concentrated polycations-functionalized graphene nanosheets with excellent solubility and stability, and its fast, facile and controllable assembly of multiple nanoparticles," Nanoscale **2**(5), 663-670(2013).

79. Z. Fang, Y. Wang, J. Song, Y. Sun, J. Zhou, R. Xu, and H. Duan, "Immobilizing CdS quantum dots and dendritic Pt nanocrystals on thiolated graphene nanosheets toward highly efficient photocatalytic H2 evolution," Nanoscale **20**(5), 9830-9838 (2013).

80. X. R. Li, M. C. Xu, H. Y. Chen, and J. J. Xu, "Bimetallic Au-Pt-Au core-shell nanoparticles on graphene oxide nanosheets for high-performance bi-directional sensing," J. Mater. Chem. B **15**(3), 4355-4362 (2015).

81. X. Huang, Z. Zeng, S. Bao, M. Wang, X. Qi, Z. Fan, and H. Zhang, "Solution-phase epitaxial growth of noble metal nanostructures on dispersible single-layer molybdenum disulfide nanosheets," Nat. Commun. **4**, 1444-1448 (2013).

82. Y. Zhang, J. Yan, X. Ren, L. Pang, H. Chen, and S. (Frank) Liu, "2D WS2 nanosheet supported Pt nanoparticles for enhanced hydrogen evolution reaction," Int. J. Hydrogen Energy **8**(42), 5472-5477 (2017).

83. L. A. Porter, H. C. Choi, A. E. Ribbe, and J. M. Buriak, "Controlled Electroless Deposition of Noble Metal Nanoparticle Films on Germanium Surfaces," Nano Lett. **2**(10), 1067-1071 (2002).

84. T. Osaka, T. Misato, J. Sato, H. Akiya, T. Homma, M. Kato, Y. Okinaka, and O. Yoshioka, "Evaluation of Substrate (Ni)-Catalyzed Electroless Gold Plating Process," J. Electrochem. Soc. **147**(3), 1059 (2002).

85. J. H. Byeon and J. T. Roberts, "Silver deposition on a polymer substrate catalyzed by singly charged monodisperse copper nanoparticles," ACS Appl. Mater. Interfaces **4**(5), 2515-2520 (2012).

86. T. L. Tan, L. L. Wang, J. Zhang, D. D. Johnson, and K. Bai, "Platinum nanoparticle during electrochemical hydrogen evolution: Adsorbate distribution, active reaction species, and size effect," ACS Catal. **5**(4), 2376-2383 (2015).

87. W. S. M. Werner, K. Glantschnig, and C. Ambrosch-Draxl, "Optical constants and inelastic electron-scattering data for 17 elemental metals," J. Phys. Chem. Ref. Data **38**(4), 1013-1092 (2009).

88. H. E. Nelson, "Radiant energy transfer in fire protection engineering problem solving," Fire Technol. **4**(3), 196-205 (1968).

89. I. Capek, "Precursors and Their Conjugates," in *Noble Metal Nanoparticles: Preparation, Composite Nanostructures, Biodecoration, and Collective Properties* (Springer Japan, 2017) pp. 136-171.

90. X. Li, L. Zhang, X. Zang, X. Li, and H. Zhu, "Photo-Promoted Platinum Nanoparticles Decorated MoS_2 Graphene Woven Fabric Catalyst for Efficient Hydrogen Generation," ACS Appl. Mater. Interfaces **8**(17), 10866-10873 (2016).

91. M. Seeram, G. T. Forcherio, and D. K. Roper, "Shape Generator for the DDSCAT software," University of Arkansas (2015).

92. A. D. Rakic, A. B. Djurisic, J. M. Elazar, and M. L. Majewski, "Optical properties of metallic films for vertical-cavity optoelectronic devices.," Appl. Opt. **22**(37), 5271-5283(1998).

93. Y. Li, A. Chernikov, X. Zhang, A. Rigosi, H. M. Hill, A. M. Van Der Zande, D. A. Chenet, E. M. Shih, J. Hone, and T. F. Heinz, "Measurement of the optical dielectric function of monolayer transition-metal dichalcogenides: MoS2, Mo S e2, WS2, and WS e2," Phys. Rev. B - Condens. Matter Mater. Phys. **90**(20), 1-6 (2014).

94. S. Kessentini, D. Barchiesi, C. D'Andrea, A. Toma, N. Guillot, E. Di Fabrizio, B. Fazio, O. M. Maragó, P. G. Gucciardi, and M. Lamy De La Chapelle, "Gold dimer nanoantenna with slanted gap for tunable LSPR and improved SERS," J. Phys. Chem. C **118**(6), 3209-3219 (2014).

95. R. D. Near, S. C. Hayden, R. E. Hunter, D. Thackston, and M. A. El-Sayed, "Rapid and efficient prediction of optical extinction coefficients for gold nanospheres and gold nanorods," J. Phys. Chem. C **117**(45), 23950-23955 (2013).

96. Y. Chen, R. E. Palmer, and J. P. Wilcoxon, "Sintering of passivated gold nanoparticles under the electron beam," Langmuir **22**(6), 2851-2855 (2006).

97. I. Romero, J. Aizpurua, G. W. Bryant, and F. J. García De Abajo, "Plasmons in nearly

touching metallic nanoparticles: singular response in the limit of touching dimers," Opt. Express **14**(21), 9988 (2006).

98. G. T. Forcherio, D. DeJarnette, M. Benamara, and D. K. Roper, "Electron Energy Loss Spectroscopy of Surface Plasmon Resonances on Aberrant Gold Nanostructures," J. Phys. Chem. C **120**(43), 24950-24956 (2016).

99. G. Liu, H. Deng, G. Li, L. Chen, Q. Dai, S. Lan, and S. Tie, "Nonlinear Optical Properties of Large-Sized Gold Nanorods," Plasmonics **9**(6), 1471-1480 (2014).

100. M. N. Su, Q. Sun, K. Ueno, W. S. Chang, H. Misawa, and S. Link, "Optical Characterization of Gold Nanoblock Dimers: From Capacitive Coupling to Charge Transfer Plasmons and Rod Modes," J. Phys. Chem. C **122**(31), 18005-18011 (2018).

101. F. Deng, H. Liu, M. Panmai, and S. Lan, "Sharp bending and power distribution of a focused radially polarized beam by using silicon nanoparticle dimers," Opt. Express **26**(16), 20051 (2018).

102. J. H. Yoon, F. Selbach, L. Schumacher, J. Jose, and S. Schlücker, "Surface plasmon coupling in dimers of gold nanoparticles: Experiment and theory for ideal (spherical) and nonideal (faceted) building blocks," ACS Photonics **6**(3), 642-648 (2019).

103. A. E. Schlather, N. Large, A. S. Urban, P. Nordlander, and N. J. Halas, "Near-field mediated plexcitonic coupling and giant Rabi splitting in individual metallic dimers," Nano Lett. **13**(7), 3281-3286 (2013).

104. J. R. Dunklin, P. Lafargue, T. M. Higgins, G. T. Forcherio, M. Benamara, N. McEvoy, D. K. Roper, J. N. Coleman, Y. Vaynzof, and C. Backes, "Exploiting the redox edge chemistry of liquid-exfoliated 2H-WS2 to yield highly monolayer-rich gold decorated nanosheets in dispersion," NPJ **1**(10), 23-35 (2018).

105. A. Slablab, L. Le Xuan, M. Zielinski, Y. de Wilde, V. Jacques, D. Chauvat, and J.-F. Roch, "Second-harmonic generation from coupled plasmon modes in a single dimer of gold nanospheres," Opt. Express **20**(1), 220 (2011).

106. H. Tamaru, H. Kuwata, H. T. Miyazaki, and K. Miyano, "Resonant light scattering from individual Ag nanoparticles and particle pairs," Appl. Phys. Lett. **80**(10), 1826-1828 (2002).

107. L. Gunnarsson, T. Rindzevicius, J. Prikulis, B. Kasemo, M. Käll, S. Zou, and G. C. Schatz, "Confined plasmons in nanofabricated single silver particle pairs: Experimental observations of strong interparticle interactions," J. Phys. Chem. B **109**(3), 1079-1087 (2005).

108. T. Atay, J. H. Song, and A. V. Nurmikko, "Strongly interacting plasmon nanoparticle pairs: From dipole-dipole interaction to conductively coupled regime," Nano Lett. **4**(9), 1627-1631 (2004).

109. P. B. Johnson and R. W. Christy, "Optical constants of the noble metals," Phys. Rev. B **6**(12), 4370-4379 (1972).

110. M. Pitkonen, "Polarizability of a pair of touching dielectric spheres," J. Appl. Phys.

103(10), 10-17 (2008).

111. A. A. Lalayan, K. S. Bagdasaryan, P. G. Petrosyan, K. V. Nerkararyan, and J. B. Ketterson, "Anomalous field enhancement from the superfocusing of surface plasmons at contacting silver surfaces," J. Appl. Phys. **91**(5), 2965-2968 (2002).

112. A. V. Paley, A. V. Radchik, and G. B. Smith, "Quasistatic optical response of pairs of touching spheres with arbitrary dielectric permeability," J. Appl. Phys. **73**(7), 3446-3453 (1993).

113. I. W. McAllister, "The axial dipole moment of two intersecting spheres of equal radii," J. Appl. Phys. **63**(6), 2158-2160 (1988).

114. A. I. Fernández-Domínguez, S. A. Maier, and J. B. Pendry, "Collection and concentration of light by touching spheres: A transformation optics approach," Phys. Rev. Lett. **105**(26), 2-5 (2010).

115. N. Geuquet, L. Henrard, F. J. Garcı, and D. Abajo, "Two-Dimensional Quasistatic Stationary Short," Nano Letters **10**(3), 902-907 (2010).

116. A. Gloter, A. Douiri, M. Tencé, and C. Colliex, "Improving energy resolution of EELS spectra: An alternative to the monochromator solution," Ultramicroscopy **96**(3-4), 385-400 (2003).

Appendices

A: Description of Research for Popular Publication

Enhancing the alternative energy and reducing the lives cancer takes are keen motivations that many scientists use to accomplish multiple scientific milestones. The past decades the scientific community has made several breakthroughs for both healthcare and alternative energy. For example, solar and electrochemical cells have recently seen an increase in the production of power by implementing nanostructures into the designs. Also, the medical community has applied nanostructures to expedite the transport of certain drugs within a human body. These two distinct fields have seen huge success in the last decades. However, we are still dependent on fossil fuels, and cancer is still one of the deadliest diseases. Ricardo R. Romo, a Master's student in Microelectronics-Photonics at the University of Arkansas, continually asks how one can support the global energy demand with improving the alternative energy and at the same time find methods to help mitigate cancer.

Romo and his advisor, Dr. D. Keith Roper, have envisioned in discovering methods to make alternative energy and tumor ablations more efficient with nanotechnology. In order for this improvement of efficiency to happen, the unique optical properties from noble metals (platinum and gold) and semiconductors (WS_2) need to be combined. In the nanophotonics lab at the University of Arkansas, Romo and his colleague Keith Berry have successfully united these to properties by a simple and unique chemical reaction. When shining strong light on these combined materials, the optical emissions from these materials can then be converted into electricity. This electricity can be inexpensively generated with the sun as the strong light. Alternatively, the combined materials have been proven to be useful as a catalyst for the production of hydrogen fuel.

Additionally, Romo and collaborators looked at using nanostructure materials for assisting in tumor ablations. Current medical practices have used cylindrical shaped nanostructures to ablate mass tumor cells. They displace the nanostructures on the malignant mass and then shine them with visible to infrared light. The surrounding areas of the nanostructures become hot at the localized surface. This generated heat is strong enough to destroy the malignant cells. In Roper's research lab, several computational designs of these nanostructures were performed to investigate the optimal dimensions to attain the optical features in the near infrared region. They have discovered that a combination of two spheres can perform the needed optical frequencies for tumor ablations. However, these discoveries became more promising due to the nontoxic morphology that spherical shapes have when compared to the cylindrical counterparts.

With the gradual steps done in the nanophotonics lab, Romo was able to demonstrate the enhanced optical features from the combination of noble metals with semiconductors. Now with the proven enhancements, Romo is currently asking the question on how to implement these innovative optical features for the macroscale of industry. An experiment to use these combined nanostructures as a catalyst for hydrogen fuel production can be promising for future results.

B: Executive Summary of Newly Created Intellectual Property

Below is a list of newly created intellectual items.

1. Creation of Excel sheet that combines all dimer spectra to create super spectra comparable to experimental spectra.

C: Possible Patent and Commercialization Aspects of Intellectual Property

C.1 Patentability of Intellectual Property

Each of the following items was considered for potential patentability. It was decided that none of the above items could be patented. Detailed descriptions follow.

1. The Excel sheet has all of the computational spectra for 14, 15, and 16 nm diameter for Au dimers, and the modified column that combines and divides individual spectra to desired percentages. However, the Excel sheet is only good for gold nanodimers with an AuNS diameter of 14, 15, and 16 nm. This will not be suitable for other diameters, hence making it not patentable.

C.2 Commercialization Aspects

Each of the following items was considered for commercialization opportunities. It was decided that none of the above items could have commercial appeal. Detailed descriptions follow.

1. The Excel sheet for the specific dimers does not hold potential for commercialization due to it only being used for specific AuNSs of 14, 15, and 16 nm diameter. To hold commercial appeal, it should include the ability to change the diameter for alternative AuNS diameters.

C.3 Possible Future Disclosure of Intellectual Property

1. The Excel sheet for combined dimer spectra is currently being prepared for publications in the Journals of Optics Express. The first authorship will belong to Ricardo Romo and Keith Roper with multiple co-authors.

D: Broader Impact of Research

D.1 Applicability of Research Methods to Other Problems

All of the ideas and concepts discussed in this thesis could be applied to areas such as biological sensors, electrochemical co-catalysts, solar cells, and other optoelectronic devices. For example, the Pt-WS_2 (L) heterostructure could easily be produced into a co-catalyst to improve the hydrogen production via HER. Additionally, the sub-25 nm Au dimers coated with citrate could be used instead of the toxic AuNRs for tumor ablations.

D.2 Impact of Research Results on U.S. and Global Society

This research has the potential to reduce the cancer threat that takes eight million lives yearly. Recently, nanotechnology has demonstrated promise for cancer therapy through noninvasive ablation on diseased tumor cells via light-activated therapies. Current problems of this therapy arise with toxic gold nanorods, which use hazardous CTAB coating. The overlapping AuNSs have optically demonstrated visible to near infrared region (NIR) features and have a non-toxic coating of citrate, which outperforms the current AuNRs. Finding the optimal dimer dimensions in the cleft region would ultimately improve the SPR of the nanostructure. In particular, simulations determined the cleft depth to overlapping distance ratio that imposes an optimal dimer dimension that can induce a NIR region optical feature. These distinguishing features in merged AuNSs have the potential to broaden the medical community use of alternative nontoxic nanostructures for tumor mitigations.

D.3. Impact of Research Results on the Environment

The arising optical features from noble metal-noble metal (i.e. dimers) and noble metal-semiconductors heterostructures have the potential to be used in for alternative energies systems (e.g., co-catalyst for HER, surface coating for solar cell). These implementations of

nanostructures onto alternative energies could help eliminate a portion of green-house gas emissions. Effects deemed detrimental to the environment from nanoparticles escaping their host matrix have yet to be reported.

E: Microsoft Project for M.S. MicroEP Degree Plan

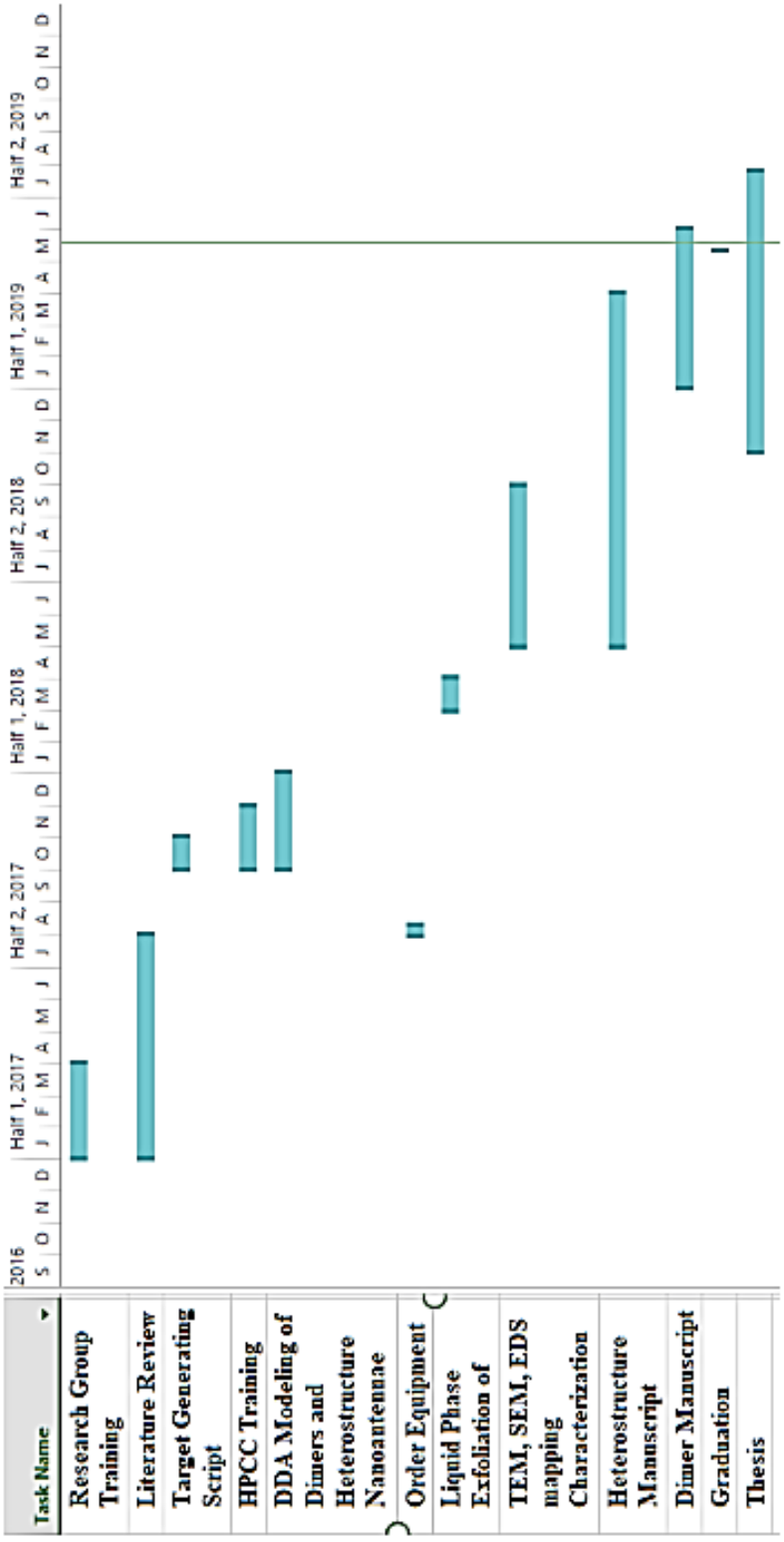

F: Identification of All Software Used in Research and Thesis Generation

Computer #1
- Model: Dell Precision T3500
- Serial Number DCRB3L1
- Location: Institute for Nanoscience and Engineering, Room 301
- Owner: NanoBio Photonics Lab, University of Arkansas

Software #1
- Name: Microsoft Office, Professional 2016
- Purchased By: Department of Chemical Engineering, University of Arkansas
- License: 02260-018-0000106-48503

Software #2
- Name Mendeley (v. 1803)
- Purchased by: Ricardo R. Romo
- License: Freeware

Software #3:
- Name: Matlab R2015b (v. 8.6.0.267246)
- Purchased By: Department of Chemical Engineering, University of Arkansas
- License: 601103

Computer #2
- Model: 15-r015x
- Serial Number: CND4193LPN
- Location: Home
- Owner: Ricardo R. Romo

Software #1
- Name: Microsoft Office, Student 2018
- Purchased By: Ricardo R. Romo
- License: 00201-10029-87936-AA359

G: All Publications Published, Submitted, and Planned

Publications Submitted

1 K. R. Berry Jr., R. L. Romo, M. Mitchell, V. Bejugam, and D. K. Roper, “Controlled Gold Nanoparticle Placement into Patterned Polydimethylsiloxane Thin Films via Directed Self-Assembly” Journal of Nanomaterials

Publications Planned

2 R. L. Romo, K. R. Berry Jr., and D. K. Roper, “Sub-25 nm gold nanosphere dimers and its interparticle junction features” Optics Express